remote sensing

MDPI

Article

Contrasting Vegetation Productivity Responses to Four Compound Temperature and Soil Moisture Extremes Across China

Pengfei Li [1], Shuzhe Huang [2], Ran Liu [1,*], Wang Gao [1], Fan Zhang [1] and Chao Wang [2]

[1] Yunnan Provincial Mapping Institute, Kunming 650034, China; qazlipengfei@126.com (P.L.); vvme@whu.edu.cn (W.G.); zhfanwhu@163.com (F.Z.)
[2] State Key Laboratory of Information Engineering in Surveying, Mapping and Remote Sensing, Wuhan University, Wuhan 430079, China; szhuang@whu.edu.cn (S.H.); c.wang@whu.edu.cn (C.W.)
* Correspondence: liuran0602@126.com

Highlights

What are the main findings?

- Wet–cold events occurred most frequently, whereas dry–hot events produced the largest GPP losses and longest conditional recovery times.
- Wet–cold events caused greater GPP losses than dry–cold events despite a lower probability of negative responses.

What are the implications of the main findings?

- Ecological risk cannot be assessed from event frequency alone because response probability, productivity loss, and recovery each require separate assessment.
- Regional monitoring should distinguish areas vulnerable to large productivity losses from those prone to prolonged vegetation recovery.

Abstract

Compound temperature and soil moisture extremes threaten terrestrial carbon uptake, but their contrasting ecological impacts remain poorly understood. We assessed dry–hot (DH), wet–hot (WH), dry–cold (DC), and wet–cold (WC) events across China from 2001 to 2025. The analyses combined daily air temperature, root-zone soil moisture, and MODIS-derived gross primary productivity (GPP). We quantified event occurrence, negative-response probability, cumulative GPP loss, and recovery time, and examined environmental predictors using explainable machine learning. WC events were most frequent, whereas DH events lasted longest. WH frequency increased over the study period, while DC frequency declined. DH and DC produced negative GPP responses in 63.5% and 67.1% of classifiable events, respectively. Among negative-response events, DH had the largest national mean cumulative event-period GPP loss below the −0.5 SD threshold (2.85 g C m^{-2}) and the longest conditional recovery time (3.17 days). WC losses exceeded DC losses despite a lower negative-response probability. Losses varied with elevation, season, and event severity. Vapor pressure deficit dominated predictions of DH negative responses and losses, whereas other event types showed greater contributions from radiation, precipitation, and soil texture. These findings highlight the need to distinguish event occurrence, response probability, productivity loss, and recovery when assessing ecological risks from compound extremes.

Check for updates

Academic Editor: Clement Atzberger

Received: 15 October 2026
Revised: 2 November 2026
Accepted: 3 November 2026
Published: 4 November 2026

Copyright: © 2026 by the authors. Licensee MDPI, Basel, Switzerland. This article is an open access article distributed under the terms and conditions of the Creative Commons Attribution (CC BY) license.

Keywords: compound hydroclimatic extremes; gross primary productivity; vegetation recovery; soil moisture; China

1. Introduction

Terrestrial vegetation removes large quantities of carbon dioxide from the atmosphere through photosynthesis, and variation in gross primary productivity (GPP) therefore exerts a major influence on the land carbon sink and its interannual variability [1–3]. This carbon uptake is jointly regulated by temperature and water availability rather than by either factor in isolation [4,5]. High temperature can directly impair photosynthetic processes while increasing atmospheric evaporative demand, whereas low soil moisture restricts root water uptake and promotes stomatal closure [6,7]. Cold conditions constrain enzymatic activity and seasonal growth, while excessive soil moisture may reduce root-zone aeration and often coincides with low solar radiation [8,9]. Since thermal and moisture anomalies frequently occur together, their ecological effects depend on the particular combination and on the environmental background in which it occurs [10,11]. Compound-event analysis has consequently become central to climate-risk research because co-occurring drivers can produce impacts that differ from those expected from the constituent anomalies alone [12,13]. For vegetation, the four combinations of anomalously high or low temperature and anomalously dry or wet soil define dry–hot (DH), wet–hot (WH), dry–cold (DC), and wet–cold (WC) events. Treating these combinations within a common framework is essential for determining how contrasting hydroclimatic states alter terrestrial productivity [14,15].

Research on compound climate impacts has nevertheless concentrated mainly on dry–hot events [16]. This emphasis is well founded because soil drying suppresses evaporative cooling, enhances surface warming, and can reinforce atmospheric aridity, while heat accelerates plant water loss and intensifies soil-moisture stress [17]. Their concurrence has been associated with widespread reductions in vegetation activity, carbon uptake, and ecosystem stability [18,19]. Far less is known about the other hydroclimatic combinations. Under wet–hot conditions, ample soil water may sustain transpiration and partly offset heat stress, but high temperature, excessive moisture, cloud-related radiation deficits, or waterlogging can still depress photosynthesis [20]. Dry–cold events combine low-temperature constraints with limited soil water, whereas wet–cold events may impose simultaneous thermal and aeration limitations [21]. Their net effects may therefore shift in direction and magnitude across climates, vegetation types, and seasons. Existing comparisons have often focused on selected event classes, individual regions, or croplands, and many assessments still characterize hydroclimatic stress using precipitation-based drought metrics rather than the root-zone moisture directly available to plants [22]. As a result, a comprehensive assessment of all four temperature and soil-moisture combinations across major terrestrial ecosystems remains lacking.

A further question is whether the four hydroclimatic combinations rank similarly across different dimensions of vegetation impact. Event frequency describes climatic exposure, the probability of a negative GPP response describes how often an eligible event is accompanied by a decline, and conditional cumulative loss describes the magnitude of loss among events classified as negative responses. These quantities are not interchangeable: a common event type may have a relatively low probability of a decline, and a high probability of decline need not imply a large conditional loss [23,24]. Recovery provides an additional dimension by describing the persistence of a response after an identifiable decline [25–27]. Comparing DH, WH, DC, and WC using consistent definitions can establish whether their rankings agree across these dimensions and how the contrasts vary among ecosystems. It can also reveal

whether the relationships observed for DH events extend to other temperature–moisture combinations. Such comparisons connect event prevalence with ecological response and help distinguish frequent exposure from large losses when negative responses occur.

The interpretation of these comparisons also depends on how compound events are defined. Climate-percentile thresholds determine the rarity of the selected temperature and root-zone soil-moisture conditions and can alter event frequency, duration, and the sample available for estimating ecological impacts. The reference period defines the background distribution against which anomalies are evaluated. Changing this period may shift event membership where climatic conditions vary over time. Seasonal treatment is equally relevant because a value that is unusual for one time of year may be typical at another. Here, local calendar-day percentiles are estimated using a circular 15-day window over the fixed 2001–2025 reference period, so each event represents a departure from the local seasonal climate. These relative thresholds do not imply that every hot, cold, dry, or wet event crosses an absolute physiological stress threshold. Ecological responses must therefore be evaluated from GPP, and their sensitivity to the climate thresholds must be distinguished from the assumptions associated with the reference period and seasonal window.

China provides a suitable region for examining these questions because its vegetated land spans pronounced gradients in climate, aridity, topography, phenology, and vegetation composition. Using daily air temperature, root-zone soil moisture, and GPP estimates for 2001–2025, we compare DH, WH, DC, and WC events across this environmental range. We ask whether the most frequent event types also have the highest probability of a negative GPP response; whether the ranking by response probability agrees with that by conditional cumulative loss; and how these contrasts and subsequent recovery vary among climate regions, vegetation types, phenological stages, and event severities. By distinguishing event prevalence from ecological susceptibility, damage, and recovery within one analytical framework, this study provides a more complete basis for evaluating compound hydroclimatic risks to vegetation productivity across China.

2. Materials and Methods

2.1. Study Area

This study covered the terrestrial area of China, extending from approximately 73.35°E to 135.25°E and from 18.05°N to 53.75°N (Figure 1). China spans pronounced gradients in climate, topography, and ecosystem structure [28]. Humid monsoon regions dominate much of the south and east, continental water limitation intensifies toward the northwest, and the Tibetan Plateau creates extensive cold, high-elevation environments [29]. These contrasts produce distinct combinations of thermal and soil-moisture conditions, providing a natural setting for comparing compound dry–hot, wet–hot, dry–cold, and wet–cold events [30]. Vegetation ranges from forests and croplands in humid regions to grasslands and sparse vegetation across arid and plateau environments. The climatic constraints on GPP and the capacity of vegetation to recover after an event can therefore differ substantially across the country.

2.2. Data

2.2.1. Remote Sensing and Derived Vegetation Data

Vegetation productivity was represented by the Daily FluxSat GPP of biomass over Land, Based on MODIS Terra and Aqua adjusted reflectance Collection 6.1 product (hereafter MODIS-GPP) [31,32]. This product provides spatially continuous daily GPP estimates and associated uncertainties at a spatial resolution of 0.05°. We used data from 2001 to 2025 to match the common study period. MODIS-GPP was developed by training neural networks with GPP estimates from 125 selected eddy covariance sites in the FLUXNET2015 and

AmeriFlux beta ONEFlux datasets. The trained relationships were subsequently applied to MODIS Collection 6.1 nadir bidirectional reflectance distribution function-adjusted reflectance (NBAR) observations from the Terra and Aqua satellites, using spectral bands 1–7. The top-of-atmosphere photosynthetically active radiation (PAR), calculated from latitude and day of year, was also incorporated to represent seasonal variation in potential radiation availability. By linking satellite observations of canopy reflectance with tower-constrained carbon uptake, MODIS-GPP provides daily productivity estimates suitable for examining vegetation responses during and after compound hydroclimatic events.

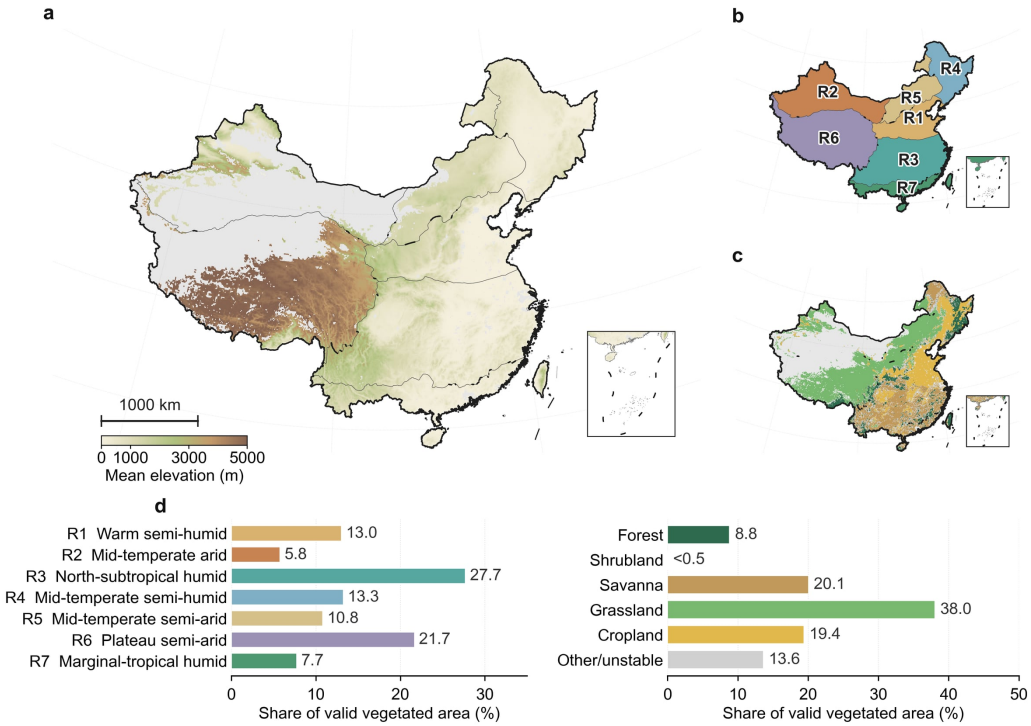


Figure 1. Study area and environmental stratification of vegetated land across China. (**a**) Shows mean elevation within the vegetation analysis domain. (**b**) Presents the seven climate regions, including the warm-temperate semi-humid region (R1), mid-temperate arid region (R2), north-subtropical humid region (R3), mid-temperate semi-humid region (R4), mid-temperate semi-arid region (R5), plateau-temperate semi-arid region (R6), and marginal tropical humid region (R7). (**c**) Shows the spatial distribution of stable vegetation classes and other or unstable vegetation. (**d**) Reports the proportion of valid vegetated area represented by each climate region and vegetation class.

Annual land cover was obtained from the 500 m MODIS MCD12Q1 product [33]. MCD12Q1 combines observations from the Terra and Aqua satellites and provides annual global land-cover classifications under several classification schemes. We used the LC_Type1 layer based on the International Geosphere–Biosphere Programme classification, which distinguishes 17 land-cover classes encompassing natural vegetation, human-modified land, and non-vegetated surfaces. Categorical land-cover data were aggregated using the modal class, while fractional coverage was calculated separately for vegetation, bare land, water, urban land, and permanent snow and ice. Stable vegetation types were determined from the dominant class during the study period and were used to examine differences in GPP responses among major ecosystem types.

2.2.2. Reanalysis and Land-Surface Data

Daily mean near-surface air temperature was obtained from ERA5-Land [34]. ERA5-Land is produced by replaying the land component of the European Centre for Medium-

Range Weather Forecasts land-surface model using atmospheric forcing from the ERA5 reanalysis. It provides temporally continuous estimates of land and near-surface conditions at an approximate native resolution of 9 km and is distributed on a 0.1° regular grid.

Daily root-zone soil moisture was obtained from version 4.3a of the Global Land Evaporation Amsterdam Model (GLEAM) [35]. GLEAM combines satellite observations and reanalysis forcing within a land-surface modelling framework that represents rainfall interception, potential and actual evaporation, soil-water storage, and evaporative stress. The fourth-generation product provides daily global estimates at a spatial resolution of 0.1° and includes both surface and root-zone soil moisture. Compared with surface soil moisture, root-zone soil moisture integrates moisture conditions below the upper soil layer and more closely represents the water available to vegetation. Temperature and root-zone soil-moisture percentiles were combined to identify the four compound event types.

Additional meteorological variables were obtained or derived from ERA5-Land, including daily vapor pressure deficit (VPD), surface solar radiation downwards, and total precipitation. VPD represented atmospheric water demand, while solar radiation characterized the energy available for photosynthesis and evapotranspiration. Total precipitation described water inputs during each event. These variables were used to characterize event-period environmental conditions and as candidate predictors of the probability and magnitude of GPP responses.

2.2.3. Ancillary Data

Elevation was obtained from the Shuttle Radar Topography Mission digital elevation model (SRTM DEM) [36]. Soil clay, sand, and silt fractions were derived from the Harmonized World Soil Database (HWSD) [37]. These variables were aggregated to the 0.1° grid and used to characterize topographic and soil controls on spatial variations in GPP responses. All ancillary data were referenced to WGS 84 and spatially aligned with the other datasets before analysis.

2.3. Methods

2.3.1. Data Preprocessing

All datasets were aligned to the native GLEAM v4.3a 0.1° cell centers in WGS 84 (EPSG:4326). GLEAM root-zone soil moisture was extracted directly. Daily mean air temperature was bilinearly resampled using its source geotransform and converted from kelvin to degrees Celsius. The 0.05° MODIS GPP was aggregated by area-weighted averaging of valid source values, preserving units of g C m^{-2} d^{-1}. At each analysis pixel, the mean GPP for each calendar day over 2001–2025 was calculated and smoothed with a circular 15-day moving average. Pixels were retained only if the annual maximum of this smoothed climatology and its annual amplitude, defined as the maximum minus the minimum, were both at least 0.1 g C m^{-2} d^{-1}. Annual 500 m MODIS land cover was aggregated by the modal class, with fractions calculated separately as averages of valid source-cell class indicators. Daily datasets were matched by grid coordinates and date. Annual land-cover maps were processed by year and summarized over the study period. Source “nodata” and non-finite values were treated as missing, with valid zeros retained. Unclassified, fill, and other invalid land-cover codes were excluded from class and fraction calculations. Pixels were retained when each core daily variable had at least 90% valid values over 2001–2025, vegetation occupied at least 50% of valid land-cover area in at least 16 years, mean bare-ground fraction was no greater than 50%, and mean valid land-cover coverage was at least 90%.

2.3.2. Identification and Characterization of Compound Hydroclimatic Events

Dynamic percentiles were calculated separately for temperature and root-zone soil moisture at each pixel and calendar day using observations from a circular 15-day window during 2001–2025. To accommodate repeated soil-moisture values, the empirical percentile of an observation x was determined using the midrank estimator.

$$p(x) = \frac{N(x_j < x) + 0.5N(x_j = x)}{N_{valid}} \quad (1)$$

Dry–hot, wet–hot, dry–cold, and wet–cold conditions were defined by ($p_T \geq 0.85$, $p_{SM} \leq 0.15$), ($p_T \geq 0.85$, $p_{SM} \geq 0.85$), ($p_T \leq 0.15$, $p_{SM} \leq 0.15$), and ($p_T \leq 0.15$, $p_{SM} \geq 0.85$), respectively (Figure 2a). Consecutive days assigned to the same compound state constituted one event, including sequences crossing calendar years. Intervening non-event days were not bridged.

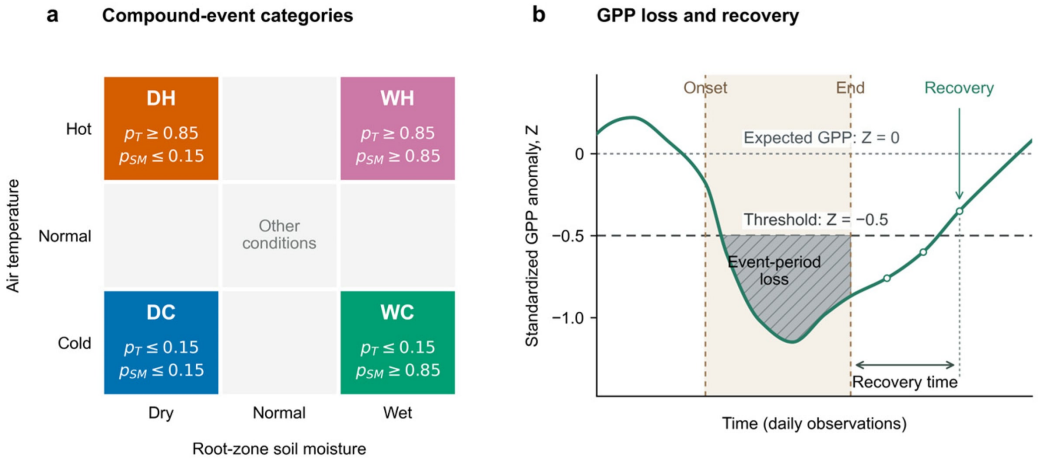


Figure 2. Definitions of compound temperature and soil-moisture events and the associated GPP response metrics. (**a**) Dry–hot (DH), wet–hot (WH), dry–cold (DC), and wet–cold (WC) states defined by daily temperature and root-zone soil-moisture percentiles. (**b**) An illustrative standardized GPP change showing the expected baseline (Z = 0) and response/recovery threshold (Z = −0.5). Hatching denotes only the below-threshold deficit within the event. Post-event deficits are excluded. Loss is calculated in original GPP units using Equations (8) and (9). Open circles illustrate daily post-event observations, and the arrow measures time from event termination to the first valid day above −0.5.

Event characteristics included frequency, duration, mean severity, and peak severity. Events were classified as moderate, strong, or extreme when their most severe joint day reached the 0.85 and 0.15, 0.90 and 0.10, or 0.95 and 0.05 thresholds, respectively. The event climatology retained one-day events, whereas GPP analyses used uncensored events lasting at least two days and beginning within the active growing season. Continuous severity was calculated from daily temperature and root-zone soil-moisture percentiles, p_T and p_{SM}, expressed on a 0–1 scale. The temperature tail score q_T was p_T for hot events and $1 - p_T$ for cold events; the moisture tail score q_{SM} was $1 - p_{SM}$ for dry events and p_{SM} for wet events. The two scores received equal weights:

$$S_{i,t} = \frac{q_{T,i,t} + q_{SM,i,t}}{2} \quad (2)$$

For an event lasting D days, from t_s to t_e, mean and peak severity were defined as

$$S_{event}^{mean} = \frac{1}{D}\sum_{t=t_s}^{t_e} S_{i,t} \quad (3)$$

$$S_{event}^{peak} = max_{t_s \le t \le t_e} S_{i,t} \quad (4)$$

These events were pooled across pixels and years within each event type, ranked by peak severity, and divided into five nearly equal-sized groups (Q1–Q5).

2.3.3. Quantification of GPP Responses, Productivity Losses, and Recovery

For each pixel, we constructed a dynamic GPP baseline accounting for both seasonal variation and the long-term trend. For each calendar day, the reference sample comprised all observations within a centered 15-day moving window from 2001 to 2025 [15]. Let $\mu_{i,d}$ denote the smoothed climatological GPP for calendar day d. A linear trend was fitted to the residual $r_{i,t} = GPP_{i,t} - \mu_{i,d}$, and expected GPP was calculated as

$$GPP_{i,t}^{exp} = \mu_{i,d(t)} + \alpha_i + \beta_i (t - 3467) \quad (5)$$

The standardized GPP anomaly was then obtained from

$$Z_{i,t} = \frac{GPP_{i,t} - GPP_{i,t}^{exp}}{\sigma_{i,d(t)}} \quad (6)$$

where $\sigma_{i,d}$ was estimated from detrended residuals within the corresponding 15-day calendar window. A negative excursion was recorded when at least one valid active-season day from event onset through three days after event termination had $Z \le -0.5$. The negative-response probability was the fraction of classifiable events meeting this criterion, which also determined the negative-event sample used in subsequent analyses. To describe the event-average response direction, a separate symmetric classification was applied to all classifiable events using mean Z over valid active-season days during the event, with negative for mean $Z \le -0.5$, neutral for $-0.5 <$ mean $Z < 0.5$, and positive for mean $Z \ge 0.5$. These mutually exclusive mean-response classes were assigned independently of the excursion criterion. Duration sensitivity was assessed using two-day events, the minimum eligible duration, with all five days from onset through termination plus three days valid and within the active season. Proportions were calculated within pixels and then area-weighted, requiring at least five classifiable events per pixel in each analysis. The negative-response probability was calculated over all classifiable events.

$$P_{neg} = \frac{N_{neg}}{N_{neg} + N_{pos} + N_{neutral}} \quad (7)$$

Productivity loss was quantified only for negative-response events. Daily loss and cumulative loss were calculated as

$$l_{i,t} = max\left(0, GPP_{i,t}^{exp} - 0.5\sigma_{i,d(t)} - GPP_{i,t}\right) \quad (8)$$

$$L_{event} = \sum_{t=t_s}^{t_e} l_{i,t} \quad (9)$$

Recovery was reached on the first day with $Z > -0.5$ [19]. Searches began one day after event termination and ended at the next compound event. Event composites extended from 15 days before to 30 days after event onset or termination.

Event frequency, event days, duration, severity, and affected area were calculated annually for each pixel. Temporal trends were estimated using the Theil–Sen slope and evaluated with the Mann–Kendall test. Regional estimates were first calculated within individual pixels and then weighted by cell area. Response heterogeneity was evaluated across event types, climate regions, stable vegetation groups, elevation bands, seasons, and event-severity classes. Differences between groups were evaluated directly using 10,000 joint bootstrap resamples of 2° spatial blocks. All eligible pixel observations within a sampled

block were retained together, and identical block multiplicities were applied to the groups being compared. Two-sided p-values were calculated from the null-centered bootstrap distribution of the difference. Holm correction was applied separately to all event-type pairs within each metric and stratum, and to all stratum pairs within each metric and event type. Differences were considered significant at adjusted $p < 0.05$.

2.3.4. LightGBM Modeling and SHAP Interpretation of Potential Environmental Predictors

Separate LightGBM models were constructed for each event type and response variable [38]. Binary classification modelled negative-response occurrence among all classifiable events. Regressions modelled cumulative GPP loss among negative-response events and recovery time among successfully recovered negative-response events. Each model used six predictors, including VPD, shortwave radiation, precipitation, elevation, and clay and sand fractions. Silt was retained for descriptive summaries but excluded from model fitting because clay, sand, and silt sum to approximately 100%.

Predictors were selected to represent atmospheric water demand, energy supply, water input, and local site conditions. VPD captures atmospheric evaporative demand associated with stomatal regulation and photosynthetic responses [39]. Radiation represents energy availability for photosynthesis and evapotranspiration, while precipitation represents water input during the event; their relevance varies with local water and energy limitation [9]. Elevation represents broad topographic gradients in climatic conditions, and soil texture characterizes differences in water retention and hydraulic transport [40].

Training and independent testing samples were separated using 2° spatial blocks, and the training blocks were divided into five spatial folds. Each model used 300 boosting iterations, a learning rate of 0.05, 31 leaves, and a minimum of 200 observations per leaf. TreeSHAP values quantified the direction and magnitude of predictor contributions. The relative predictive contribution of factor k was calculated as

$$C_k = 100 \times \frac{E_w(|\emptyset_k|)}{\sum_j E_w(|\emptyset_j|)} \quad (10)$$

where $\emptyset_k$ denotes the SHAP value and w accounts for pixel area and event frequency. Exact TreeSHAP interaction values were further used to evaluate the joint predictive association between VPD and precipitation for GPP loss.

Predictor dependence was assessed using pairwise Spearman correlations and variance inflation factors in the training samples for each event type and response. Additional ablation analyses excluded VPD or radiation from the WH cumulative GPP loss model while retaining the same response definition, samples, weights, spatial partitions, cross-validation folds, hyperparameters, and random seed. Predictive performance was compared using independent spatial testing and five-fold spatial cross-validation. SHAP comparisons used the same explanation samples and mapped event population as the full model. SHAP values were interpreted as contributions to the predictions of the fitted LightGBM models. Relative importance summarizes the allocation of weighted mean absolute SHAP contributions among the predictors. Pairwise SHAP interactions describe departures from additive SHAP main effects in the predicted response. These quantities were used to characterize predictive associations, without assigning causal effects to individual environmental factors.

3. Results

3.1. Spatiotemporal Patterns and Trends of Compound Hydroclimatic Events

To establish the hydroclimatic context for subsequent GPP analyses, we first compared the frequency, duration, and spatial distribution of the four compound event types. Across

China, these characteristics differed during 2001 to 2025. WC events occurred most frequently, with a national area-weighted mean of 6.96 events pixel^{-1} yr^{-1}, followed by DH, WH, and DC events at 5.58, 3.33, and 2.52 events pixel^{-1} yr^{-1}, respectively (Figure 3). DH events persisted longest, averaging 2.28 days per event, whereas WH events were shortest at 1.51 days. DC and WC events both lasted approximately 1.86 and 1.83 days. Thus, the most frequent event type did not represent the longest duration. DH and WC also generally exhibited higher peak severity than WH and DC, although differences in their percentile-based severity were smaller than those in frequency. Direct pairwise tests supported the national frequency ordering WC > DH > WH > DC and showed that DH events lasted longer than the other event types (all Holm-adjusted $p < 0.001$; Table S1).

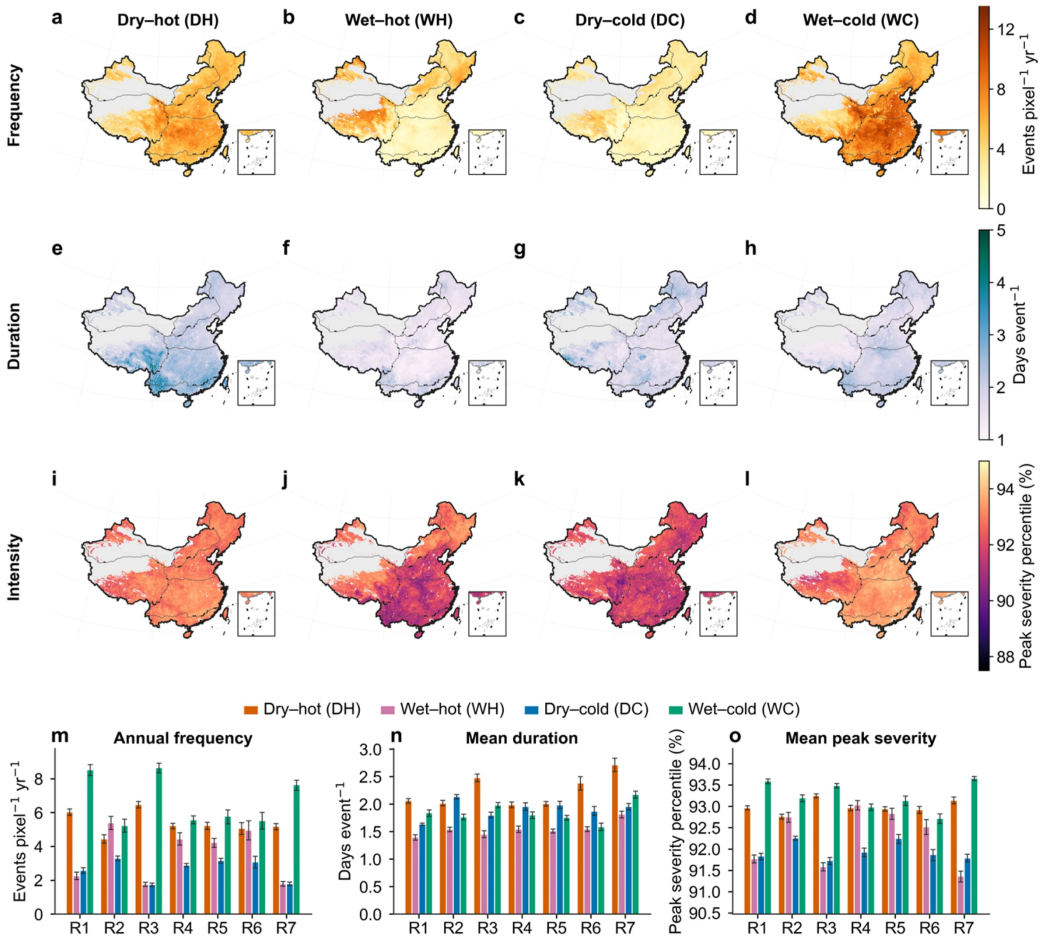


Figure 3. Spatial patterns of compound-event frequency, duration, and peak severity across China from 2001 to 2025. (**a**–**d**) Show the mean annual frequency of DH, WH, DC, and WC events. (**e**–**h**) Show the corresponding mean event duration, and (**i**–**l**) show mean peak severity. (**m**–**o**) Compare the area-weighted means of the three event characteristics across the seven climate regions. Error bars indicate 95% confidence intervals obtained from 1000 bootstrap resamples of 2° spatial blocks within each climate region.

These national-scale patterns were accompanied by pronounced regional contrasts between humid eastern China and the drier northern and plateau regions (Figure 3a–l). WC and DH frequencies peaked in the north subtropical humid region, reaching 8.64 and 6.46 events pixel^{-1} yr^{-1}, respectively. WC events were also frequent in the warm temperate semi-humid and marginal tropical humid regions. By contrast, WH events were comparatively frequent in the mid-temperate arid and plateau temperate semiarid regions, at 5.38 and 4.94 events pixel^{-1} yr^{-1}, respectively. DH duration reached 2.71 days in the

marginal tropical humid region, whereas WH duration remained below 1.9 days in every climate region (Figure 3m–o). These distributions describe departures from local seasonal conditions, so frequent wet or hot events did not necessarily identify regions with the highest absolute soil moisture or temperature [41,42].

In addition to these spatial patterns, temporal changes were most evident for event frequency (Figure 4). WH frequency increased significantly by 1.86 events pixel^{-1} yr^{-1} per decade, whereas DC frequency decreased by 0.95 events pixel^{-1} yr^{-1} per decade. DH frequency showed a positive slope of 0.41 events pixel^{-1} yr^{-1} per decade, but this change was not statistically significant, and WC frequency decreased significantly by 0.88 events pixel^{-1} yr^{-1} per decade. WH increases were particularly evident in northeastern China and parts of the plateau, while DC decreases occurred across substantial areas of northern and western China. Changes in duration and peak severity differed among event types. DH and WH duration increased by approximately 0.25 and 0.08 days per decade, respectively. DH peak severity increased by 0.33 percentage points per decade, whereas changes in peak severity remained below 0.15 percentage points per decade in magnitude for the other three event types. The principal temporal contrast was therefore an increase in WH occurrence and a decrease in DC and WC occurrence, rather than a uniform intensification of all four event types.

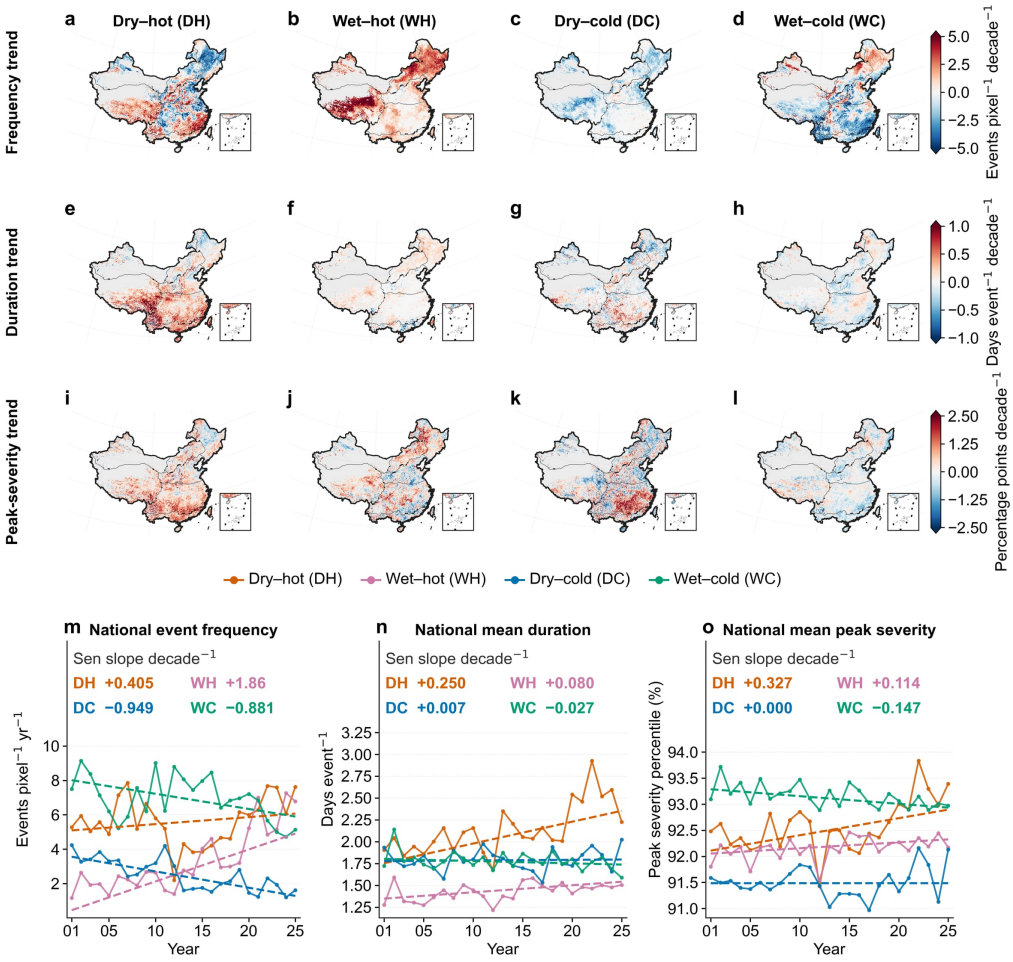


Figure 4. Spatial and temporal trends in compound-event characteristics from 2001 to 2025. (**a**–**d**) Show spatial trends in annual event frequency for DH, WH, DC, and WC events. (**e**–**h**) Present trends in mean duration, and (**i**–**l**) present trends in mean peak severity. Pixel-level trends were estimated using the Theil–Sen slope. (**m**–**o**) Show national area-weighted annual values and the corresponding Theil–Sen trends, with slopes reported per decade. Trend significance was evaluated using the Mann–Kendall test.

3.2. Contrasting GPP Response Probability, Loss, and Recovery Among Compound Event Types

To determine whether the distinct event patterns translated into differences in ecological impact, we first quantified the probability of a negative GPP response. Negative responses were most common during DC and DH events, with national area-weighted probabilities of 67.1% and 63.5%, respectively, compared with 60.1% for WC and 39.9% for WH events (Figure 5). Both DH and DC had higher negative-response probabilities than WH and WC (all Holm-adjusted $p < 0.05$). The mean probability was significantly higher for DC than for DH (67.05% versus 63.55%), with a difference of 3.50 percentage points (95% confidence interval: 1.07–5.92 percentage points; adjusted $p = 0.008$). Regional differences were substantial, particularly for the wet-event types. WC negative-response probability reached 72.1% in the plateau temperate semi-arid region but fell to 30.8% in the mid-temperate semiarid region. WH probability ranged from 22.2% in the mid-temperate semiarid region to 49.9% in the mid-temperate semi-humid region. DH probability was highest in the mid-temperate semiarid region at 79.8%, but declined to 45.8% on the plateau, where DC probability reached 72.9%. These regional reversals indicate that the same compound event type did not impose a uniform constraint across climatic settings. Stronger water limitation may amplify DH responses in semiarid regions, whereas low temperature may exert greater control over GPP on the plateau [43,44]. Under the symmetric event-mean classification, national negative, neutral, and positive proportions were 52.8%, 25.4%, and 21.8% for DH; 23.7%, 31.3%, and 45.0% for WH; 45.3%, 39.8%, and 14.9% for DC; and 38.4%, 38.7%, and 22.9% for WC. The numerical ordering of negative mean responses remained DH > DC > WC > WH. Restricting the original excursion criterion to two-day events with five valid active-season observations yielded probabilities of 63.0%, 64.8%, 56.9%, and 39.2% for DH, DC, WC, and WH, respectively, preserving the same ordering.

Among events with a negative response, the national area-weighted mean cumulative event-period GPP loss below the −0.5 SD threshold was greatest for DH at 2.85 g C m^{-2}, followed by WC, DC, and WH at 1.56, 1.15, and 0.83 g C m^{-2}, respectively (Figure 6). Cumulative GPP loss differed among all four event types, following DH > WC > DC > WH (all Holm-adjusted $p < 0.001$). The DH–WC difference was 1.28 g C m^{-2}, with a 95% confidence interval of 1.09–1.46 g C m^{-2}. DH had the greatest mean loss over 73.0% of the area where a dominant event type could be identified. This spatial pattern extended to southwestern China, including much of Yunnan, where DH events produced the largest mean cumulative GPP loss among the four event types (Figure 6e). WH-associated losses were comparatively small in this area (Figure 6b). Across climate regions, DH losses were particularly large in the mid-temperate semi-humid region, averaging 5.0 g C m^{-2}. Across stable vegetation classes, DH losses reached 3.8 g C m^{-2} in both forests and croplands. WC losses were also relatively large in forests, at 2.7 g C m^{-2}, whereas WH losses remained low across the major vegetation classes. The contrast between DC and WC was informative. DC more frequently crossed the negative-response threshold, but WC incurred greater cumulative absolute loss. The probability of a negative response and the associated carbon loss therefore captured distinct dimensions of vegetation impact [18,45]. Differences in event duration and the underlying productivity scale may contribute to this separation.

Recovery also varied among event types and environmental settings (Figure 7). The mean time to recovery among recovered negative-response events was 3.17 days for DH, 2.62 days for DC, 3.07 days for WH, and 2.30 days for WC. Of the negative-response events, 1,190,112 DH, 122,016 WH, 317,389 DC, and 1,933,683 WC events had observed recovery, accounting for 54.5%, 55.2%, 57.6%, and 85.1% of the events, respectively (Table S2). Subsequent events accounted for 92.9% of searches ending without observed recovery. On the pixels with recovered events of all four types, the conditional mean recovery times were 3.14, 3.08, 2.55, and 2.18 days for DH, WH, DC, and WC, retaining the national ordering.

DH recovery was longer than that of DC and WC (both Holm-adjusted $p < 0.001$), but the difference between DH and WH was not significant (adjusted $p = 0.361$). WH recovery was significantly longer than WC recovery (adjusted $p < 0.001$). DH recovery times ranged from 2.7 to 3.8 days across climate regions, whereas WC recovery was prolonged in both the mid-temperate arid and plateau temperate semi-arid regions. WC recovery averaged approximately 3.7 days in the plateau temperate semi-arid region and 3.8 days in the mid-temperate arid region, compared with 1.6 to 1.8 days in several humid regions. Grasslands also exhibited longer WC recovery times than forests and croplands. Persistent soil-moisture deficits may partly account for the longer recovery following DH events [19,46]. For WC events, continued temperature limitation may delay GPP recovery at high elevations even after the compound thresholds are no longer met [47].

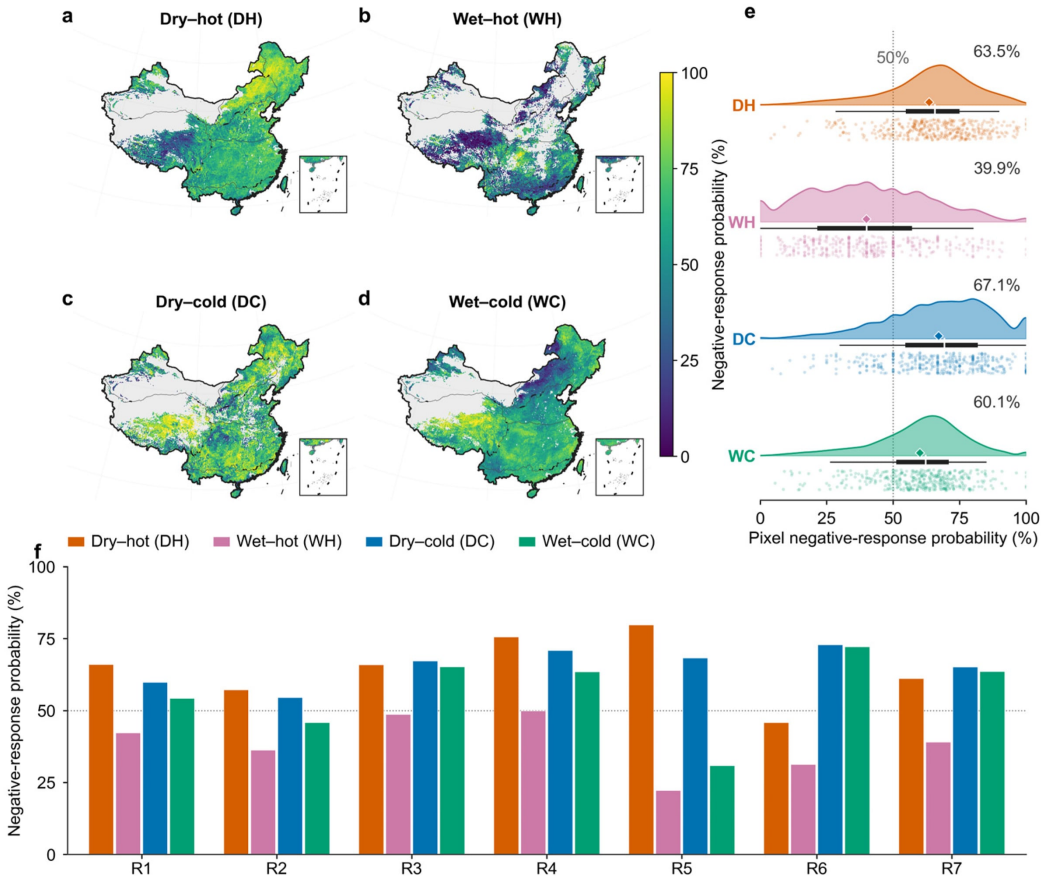


Figure 5. Probability of a negative GPP excursion to the four compound-event types. (**a**–**d**) Show the probability that a classifiable DH, WH, DC, or WC event produced a negative GPP response. (**e**) Presents the area-weighted distributions of probabilities. Thin horizontal segments represent the 5th to 95th percentiles, thick segments represent the interquartile range, white ticks indicate the median, and diamonds indicate national area-weighted means with 95% bootstrap confidence intervals. (**f**) Compares negative-response probabilities across the seven climate regions. The vertical and horizontal dotted lines in (**e**,**f**) indicate a probability of 50%.

To relate these response metrics to the temporal evolution of GPP, we further examined the composite trajectories around event onset (Figure 8). DH and DC were already associated with negative GPP anomalies before their formal onset. DH reached a minimum of approximately −0.42 standard deviations one day after onset, whereas DC reached −0.45 at onset and then gradually returned towards zero. Their negative pre-event anomalies indicate that productivity stress often developed before temperature and soil moisture simultaneously crossed the compound thresholds. The identified onset therefore marked

entry into the defined compound state rather than the beginning of the ecological response. WC exhibited a sharper but more transient decline to approximately −0.39 at onset and then rebounded to positive anomalies. The rapid rebound may have occurred as temperature limitation weakened while soil moisture remained available. WH maintained a positive mean anomaly throughout the displayed window despite its negative-response probability of 39.9%. This apparent contrast arose because classification required only one day below the negative threshold, whereas the composite averaged daily anomalies across all events. Brief negative excursions could therefore coexist with a positive mean change, indicating substantial variation among individual WH responses.

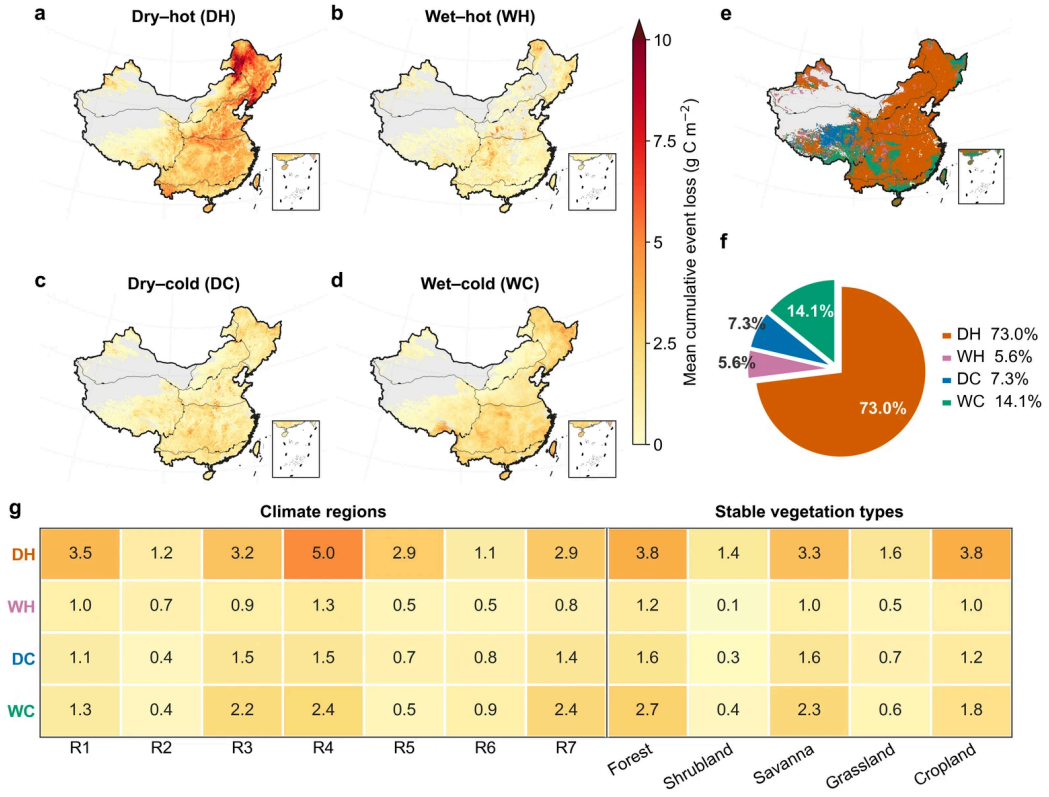


Figure 6. Spatial variation in cumulative GPP loss during negative-response compound events. (**a**–**d**) Show the mean cumulative event-period GPP loss associated with DH, WH, DC, and WC events. (**e**) Identifies the event type that produced the largest mean loss at each pixel. (**f**) Reports the proportion of mapped vegetated area dominated by each event type. (**g**) Compares mean cumulative losses across climate regions and stable vegetation classes.

3.3. Heterogeneity of GPP Responses Across Environmental Contexts and Event Severity

To determine whether the national patterns described above remained consistent across environmental settings, we compared GPP loss and conditional recovery time across elevation bands, seasons, and event severity levels. Elevation revealed a clear separation between loss magnitude and recovery dynamics (Figure 9). For each event type, cumulative loss was higher at 500–1000 m than at elevations of at least 3000 m (Holm-adjusted $p \leq 0.001$). Losses reached 3.76, 1.16, 1.44, and 1.93 g C m^{-2} for DH, WH, DC, and WC events, respectively. Above 3000 m, the corresponding values declined to 1.01, 0.49, 0.75, and 0.82 g C m^{-2}. The concentration of loss at middle elevations may partly arise from greater background productivity, which increases the absolute carbon deficit when vegetation is disturbed [4,48]. By comparison, lower productivity and shorter active seasons constrain the amount of GPP that can be lost at high elevations [49]. Recovery did not become correspondingly faster as losses declined. WC recovery increased from 1.70 days below 500 m to 3.82 days above

3000 m, while DC recovery lengthened to 3.22 days in the highest band. DH recovery varied non-monotonically with elevation, ranging from 2.89 to 3.81 days. Low temperatures and limited energy availability may delay the return to the recovery threshold at high elevations, even when the initial productivity loss is small [50].

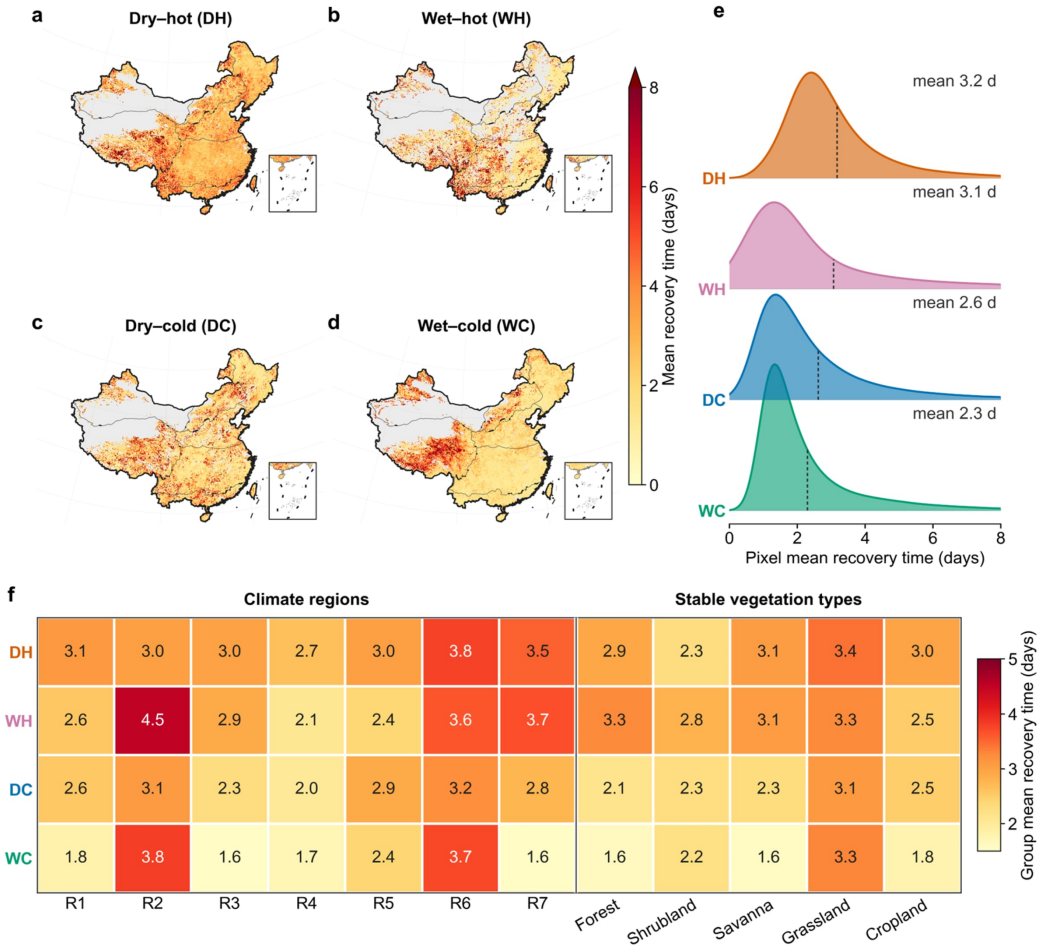


Figure 7. Spatial patterns and environmental variation in conditional GPP recovery time following compound events. (**a**–**d**) Show the mean recovery time among successfully recovered negative-response events for DH, WH, DC, and WC events. (**e**) Presents the probability density of pixel-level mean recovery time for each event type, with vertical markers indicating national means. (**f**) Compares mean recovery time across climate regions and stable vegetation classes.

Seasonal differences further separated loss magnitude from recovery timing (Figure 10). DH and WC losses peaked in summer at 3.75 and 2.03 g C m^{-2}, respectively. The summer loss associated with DH events was more than twice its winter value of 1.85 g C m^{-2}. These large summer deficits were partly related to high seasonal productivity because disturbances during peak vegetation activity translate into greater absolute carbon losses [51]. Concurrent heat and water limitation may further intensify the physiological effects of DH events during this period. DC displayed a contrasting pattern, with its greatest loss occurring in winter at 1.35 g C m^{-2}, below the corresponding DH loss. WH losses remained comparatively small throughout the year and ranged from 0.68 to 1.14 g C m^{-2}. Greater soil-water availability may have buffered part of the heat-related stress during these events [52]. Despite the summer peaks in DH and WC losses, recovery was slowest in winter for these two event types, at 3.83 and 3.06 days, respectively. WH recovery was slowest in spring at 4.21 days, whereas DC recovery was slowest in summer at 2.74 days. For DH and WC, cooler temperatures and reduced radiation can limit post-event carbon uptake and narrow the period available for

vegetation to reach its recovery threshold [47]. Consequently, the season associated with the greatest productivity loss was not necessarily the season with the longest recovery. These estimates were restricted to eligible events occurring within local active growing periods and therefore included winter conditions only where vegetation remained active.

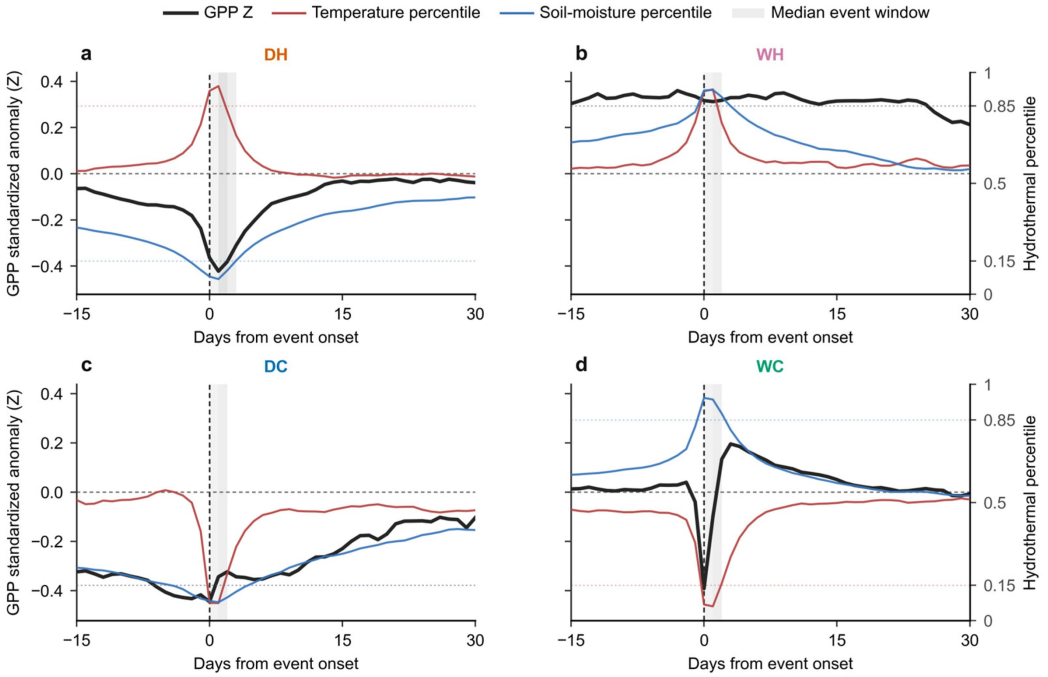


Figure 8. GPP and hydroclimatic variations around the onset of compound events. (**a**–**d**) Show variations for DH, WH, DC, and WC events from 15 days before to 30 days after onset. Black lines represent the standardized GPP anomaly, while red and blue lines represent the corresponding temperature and root-zone soil-moisture percentiles. The vertical dashed line marks event onset, and the horizontal dotted lines indicate the percentile thresholds used to identify compound conditions. Grey shading represents the typical event window, with the central interval based on median duration and the lighter extent representing variation in event termination.

Increasing event severity was associated with a higher negative-response probability for every event type (Figure 11a). Spearman correlations ranged from 0.07 to 0.30, and probabilities increased across the severity quintiles. The relationship with GPP loss was more variable (Figure 11b). DH showed the strongest association, with $\rho = 0.50$ and mean loss increasing from approximately 1.79 g C m^{-2} in Q1 to 5.30 g C m^{-2} in Q5. WC losses also increased with severity, whereas DC exhibited a weaker association. WH differed from the other types, with a modest negative relationship between severity and absolute loss, despite an increasing probability of negative response. More severe WH conditions therefore increased the likelihood of crossing the response threshold without producing greater average loss among the selected negative-response events. In contrast to the clearer changes in response probability and cumulative loss, mean recovery time varied only modestly with event severity (Figure 11c). Recovery generally lengthened toward the highest severity quintile, but the increase from Q1 to Q5 remained below half a day for every event type. DH consistently required the longest recovery, whereas WC recovered most rapidly. The limited severity dependence indicates that recovery was more strongly shaped by ecosystem state, event timing, and environmental conditions after the event than by event severity alone [53].

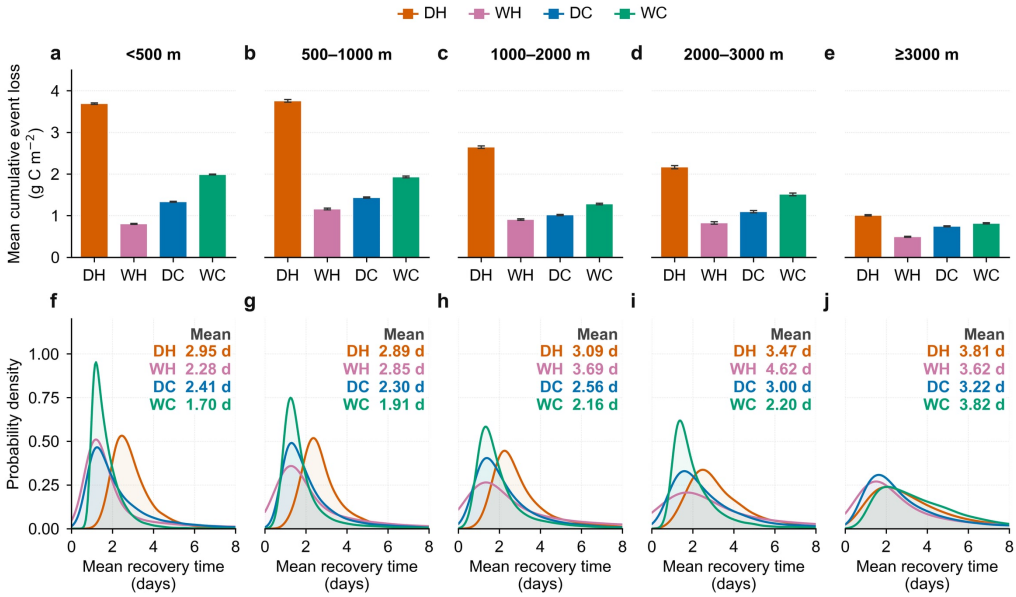


Figure 9. Elevation-dependent variation in cumulative GPP loss and conditional recovery time. (**a**–**e**) Show cumulative GPP loss for DH, WH, DC, and WC events across five elevation bands: below 500 m, 500 to 1000 m, 1000 to 2000 m, 2000 to 3000 m, and at least 3000 m. Error bars indicate 95% confidence intervals. (**f**–**j**) Show the corresponding probability density distributions of mean recovery time. Annotated values are the mean recovery times for each event type.

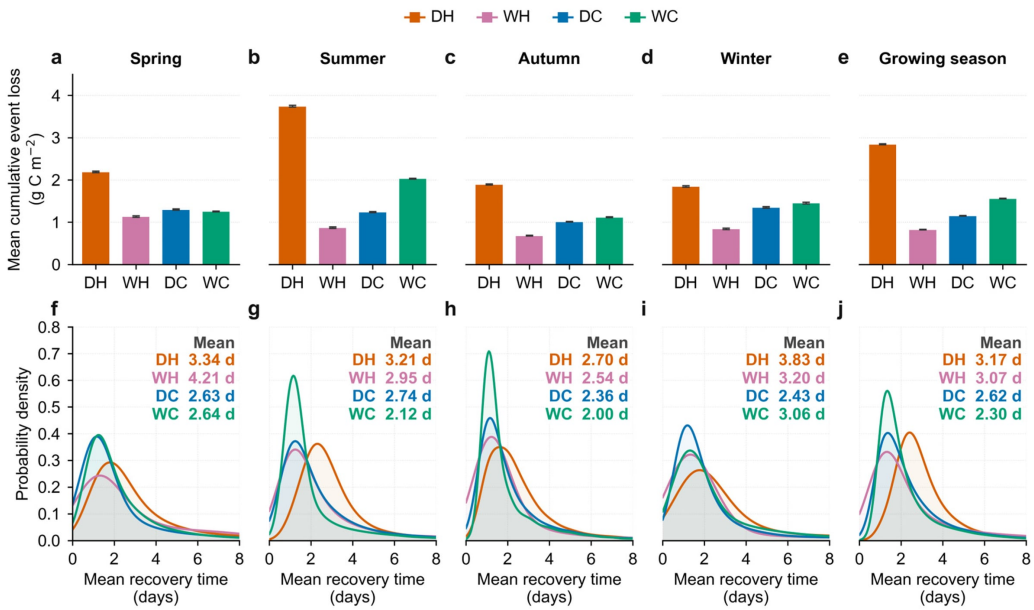


Figure 10. Seasonal variation in cumulative GPP loss and conditional recovery time. (**a**–**e**) Compare mean cumulative GPP loss among negative-response DH, WH, DC, and WC events occurring in spring, summer, autumn, winter, and the local growing season. Error bars indicate 95% confidence intervals. (**f**–**j**) Show the corresponding probability density distributions of mean recovery time, with annotated values representing the means.

3.4. Environmental Predictors of GPP Responses and Their Interactions

To identify the environmental conditions associated with the response contrasts described above, we compared the atmospheric conditions during each event type (Figure 12a–c). DH had the highest median VPD and solar radiation, at 0.91 kPa and 22.67 MJ m^{-2} d^{-1}, together with the lowest median cumulative precipitation of 1.54 mm.

WC occupied the opposite end of these distributions, with median VPD of 0.21 kPa, radiation of 10.81 MJ m^{-2} d^{-1}, and precipitation of 17.77 mm. WH and DC had similar median VPD values of approximately 0.39 kPa, but WH received substantially more precipitation. These distributions show contrasting atmospheric conditions, with higher VPD and radiation and lower concurrent precipitation for DH than for WC.

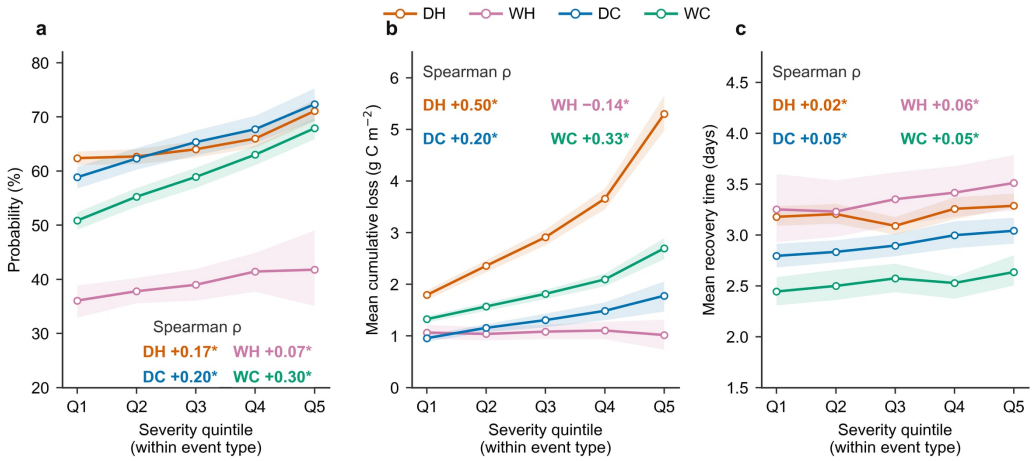


Figure 11. Relationships between compound-event severity and vegetation productivity responses. Events were ranked by peak daily joint severity within each event type and divided into five nearly equal-sized groups, Q1–Q5, before applying the response-specific filters. Estimates were calculated within pixel-quintile groups and then weighted by pixel area. (**a**) Shows negative-response probability. (**b**) Shows mean cumulative event-period GPP loss among negative-response events. (**c**) Shows mean recovery time. Shaded bands indicate 95% confidence intervals from 1000 bootstrap resamples of 2° spatial blocks. Spearman correlations were calculated across pixel and severity-class combinations. Asterisks (*) indicate statistically significant Spearman correlations after Benjamini–Hochberg correction for multiple comparisons (adjusted $p < 0.05$).

Against these contrasting environmental backgrounds, predictor contributions differed between negative-response occurrence and cumulative GPP loss (Figure 12d,e). Independent spatial testing yielded ROC-AUC values of 0.757, 0.699, 0.654, and 0.779 for negative-response classification for DH, WH, DC, and WC, respectively (Table S3). The corresponding R^2 values for cumulative GPP loss were 0.351, 0.339, 0.377, and 0.438 (Table S4). Recovery-time models explained the lower test-set variation, with R^2 values of 0.216, 0.256, 0.258, and 0.311. In the negative-response models, VPD accounted for 60.7% of the relative SHAP contribution to DH negative responses, substantially exceeding every other factor. Radiation contributed most to WH and WC negative responses, at 36.3% and 29.6%, respectively, while radiation and elevation had similar contributions for DC. In the cumulative GPP loss models, VPD remained the leading DH predictor at 34.8%, followed by soil texture at 24.5% and precipitation at 23.7%. Soil texture had the largest contribution to WH loss, at 27.9%, whereas precipitation ranked first for DC and WC, contributing 33.8% and 37.7%, respectively. The strong VPD contribution to DH response occurrence indicates that atmospheric demand distinguished more responsive events within conditions already defined as dry and hot [39]. For the wet-event types, the greater contribution of radiation indicates that energy availability helped differentiate response occurrence when soil moisture was abundant [9]. These relative importance estimates represent predictive associations within each event class. Moreover, cumulative precipitation and cumulative GPP loss were calculated over the same event window, so precipitation contributions may partly contain information related to event duration.

The spatial distribution of local SHAP importance varied among event types (Figure 13). VPD was the dominant predictor in the DH loss model across 71.9% of the mapped vegetated

area, followed by soil texture at 22.6%. WH exhibited a more heterogeneous pattern, with precipitation, soil texture, and elevation dominating 38.1%, 31.8%, and 14.1% of its mapped area, respectively. Precipitation dominated DC and WC losses over 51.9% and 68.5% of their mapped areas, especially across much of eastern and southern China. The regional importance of soil texture may be related to its influence on water storage and drainage, while precipitation can modify water availability during an event. Nevertheless, these maps identify the predictor that best explained local model variation rather than a factor acting independently of other environmental conditions.

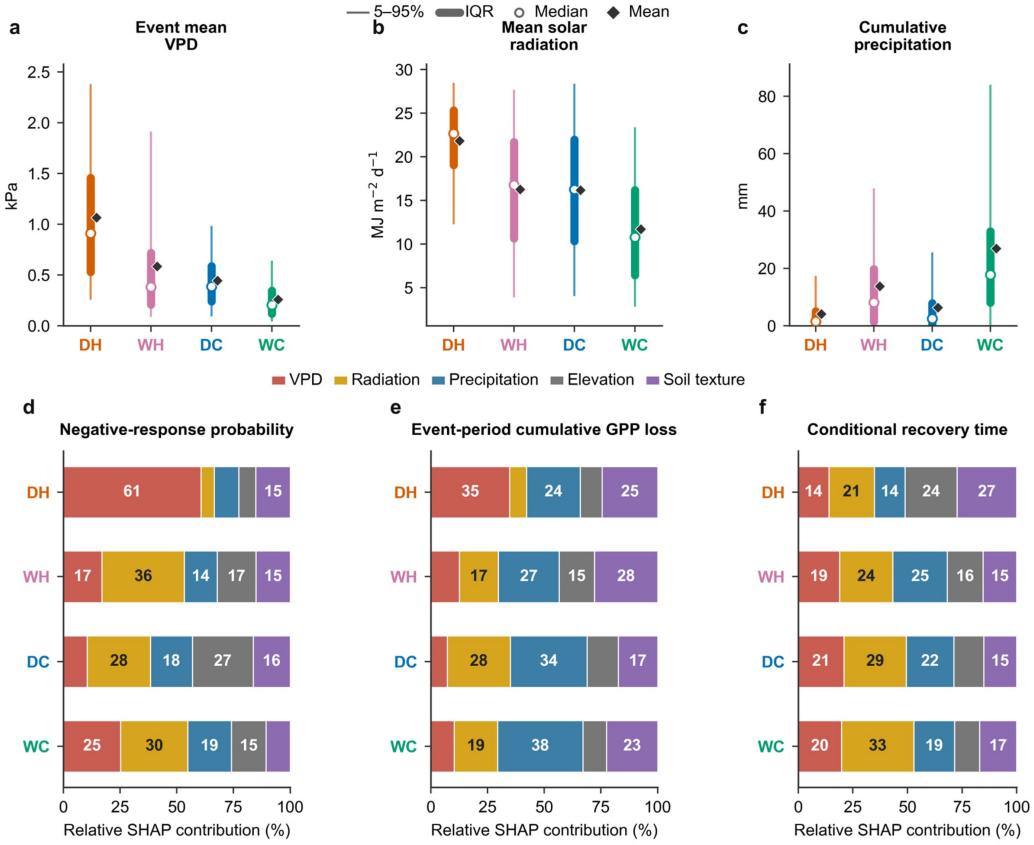


Figure 12. Hydroclimatic conditions and relative predictor contributions to modelled GPP responses. (**a**–**c**) Show the distributions of mean vapor pressure deficit, mean solar radiation, and cumulative precipitation. Thin lines represent the 5th to 95th percentiles, thick lines represent the interquartile range, circles indicate medians, and diamonds indicate means. (**d**–**f**) Show the relative SHAP importance in the models for negative-response occurrence, cumulative GPP loss and conditional recovery time. Importance was calculated from weighted mean absolute SHAP values in independent spatial test samples and sums to 100% within each model. Soil texture represents the sum of the weighted mean absolute contributions of clay and sand. Silt was included only in descriptive summaries and was not a model predictor.

VPD and precipitation also displayed interactions in predicting cumulative loss (Figure 14). Their interaction represented 15.0% of total absolute SHAP contributions for DH, compared with 6.8% for WH, 6.2% for DC, and 3.9% for WC. DH also showed the strongest variation in interaction direction across the environmental combinations. Higher VPD combined with higher precipitation generally produced positive-interaction contributions, whereas several combinations of low VPD with high precipitation or high VPD with low precipitation produced negative contributions. Across the weighted test samples, negative interactions occurred in 73.8% of DH events and 77.2% of WH events. Positive and negative interactions were nearly balanced for DC, with 50.5% positive, whereas posi-

tive interactions were more common for WC at 57.6%, although their overall interaction strengths were smaller. The stronger DH interaction indicates that predicted losses were particularly sensitive to the balance between atmospheric water demand and concurrent water input [22].

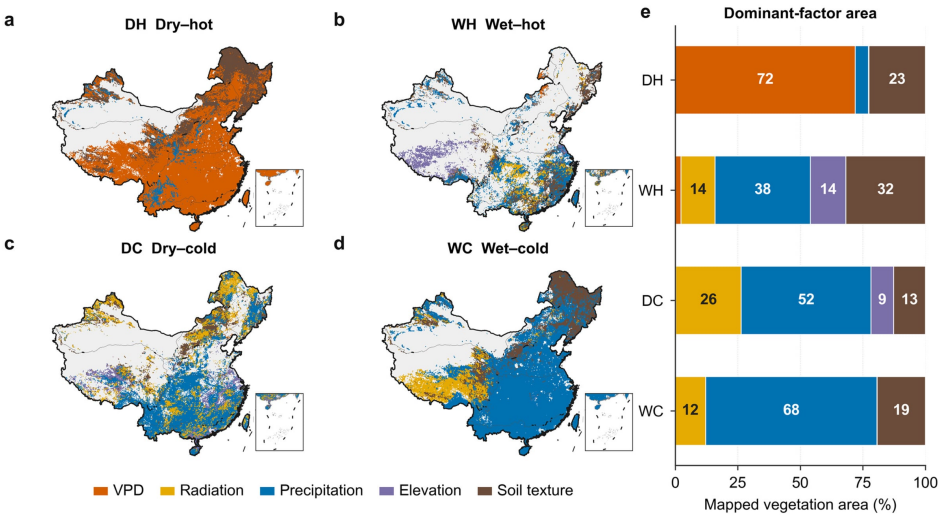


Figure 13. Spatial distribution of dominant predictors in the cumulative GPP loss models. (**a**–**d**) Show the predictor group with the largest within-cell mean absolute SHAP contribution for DH, WH, DC, and WC, respectively. The five predictor groups include vapor pressure deficit, solar radiation, cumulative precipitation, elevation, and soil texture. Dominance was determined separately at each grid cell using negative-response events. (**e**) Reports the proportion of mapped vegetated area dominated by each factor.

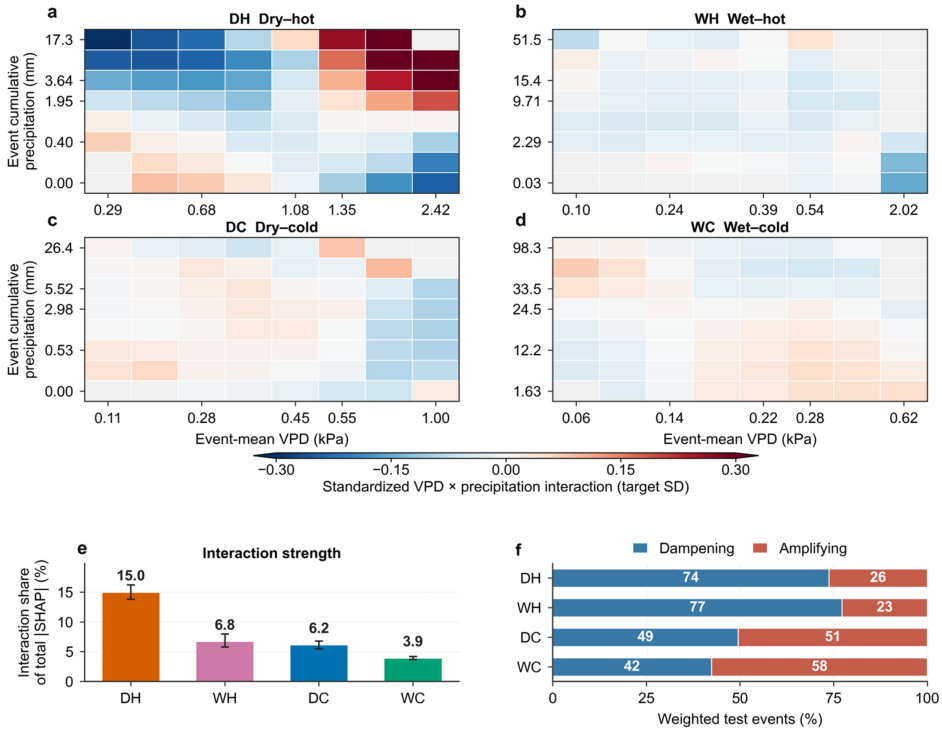


Figure 14. Predictive interaction between vapor pressure deficit and cumulative precipitation for GPP loss. (**a**–**d**) Show standardized TreeSHAP interaction values across the observed combinations of mean vapor pressure deficit and cumulative precipitation for DH, WH, DC, and WC events. Positive (amplifying) and negative (dampening) values indicate interaction contributions that increase and

decrease predicted GPP loss relative to additive SHAP main effects, respectively. (**e**) Shows the interaction magnitude as a percentage of total absolute SHAP contribution, with error bars representing 95% confidence intervals. (**f**) Shows the weighted proportions of independent test events with amplifying and dampening interactions.

4. Discussion

4.1. Contrasting GPP Responses Across Environmental Conditions

Previous studies have quantified how drought and heat, occurring individually or simultaneously, affect ecosystem carbon fluxes [54] and have established recovery time as an additional dimension of drought impact [25]. Building on the distinction between climatic drivers and ecological impacts in compound-event research [23], our analysis examines whether the same event types rank highest for exposure, negative-response probability, conditional loss, and recovery time. The contribution is an empirical comparison of these rankings across all four temperature–soil-moisture combinations under consistent analytical rules, linking the occurrence of hydroclimatic extremes to distinct aspects of vegetation response.

The national comparisons reveal contrasting response profiles (Figures 3 and 5–7). WC events were most frequent, whereas DH events had the greatest conditional loss. The DC-WC comparison further separates response occurrence from loss and recovery. DC had a higher negative-response probability, but WC had greater conditional loss and shorter observed recovery among successfully recovered events. At the event-type level, a higher probability of crossing the response threshold therefore did not imply a larger loss per negative-response event, and a larger event-period deficit did not imply slower observed recovery. These contrasts extend the assessment beyond DH impacts by identifying how cold and wet combinations differ in the likelihood, magnitude, and observed persistence of GPP decline. Considering these dimensions together reveals differences that would be missed by ranking event types using any one indicator alone.

Our analysis identified pronounced GPP reductions during DH events. In an independent analysis of global flux observations, Fu et al. (2022) found that increasing VPD was associated with lower GPP and canopy conductance across a range of soil-moisture conditions [39]. Stomatal regulation under elevated atmospheric water demand therefore provides a plausible explanation for the DH pattern observed here. However, the negative GPP anomalies preceding DH onset indicate that ecological stress often developed before temperature and soil moisture simultaneously crossed the event thresholds [55]. The identified onset therefore marks a transition into the compound state rather than necessarily the beginning of productivity decline [23]. Consequently, the entire event-period deficit should not be attributed exclusively to the compound threshold crossing.

DC events had a similarly high negative-response probability but smaller absolute losses than DH events. One possible explanation is that low temperature imposed an additional constraint on carbon assimilation under dry conditions, while differences in event duration and baseline productivity limited the accumulated carbon deficit [43,54]. More generally, a high probability of crossing a standardized anomaly threshold does not imply a large absolute loss. The former measures the occurrence of an unusual decline relative to local variability, whereas the latter also depends on the amount of carbon that vegetation would otherwise assimilate [18]. This distinction helps explain why WC events produced larger absolute losses than DC events despite a lower negative-response probability.

Wet events showed more variable ecological outcomes. WH maintained a positive mean GPP change, yet more than half of the classifiable events crossed the negative-response threshold at least once. Adequate soil moisture may buffer water stress during some hot events, while other environmental conditions constrain productivity. Excess soil moisture can itself

be associated with reduced photosynthesis, and the optimum moisture range varies among ecosystems [56]. The wet-event classification denotes relative wetness and does not diagnose soil saturation, waterlogging, or flooding. The GPP responses observed during WH and WC therefore cannot be attributed specifically to waterlogging-induced physiological stress from this classification alone. Similarly, the sharp decline and subsequent rebound during WC events are compatible with a transient environmental constraint, but the composite trajectory does not demonstrate a common recovery mechanism across all affected ecosystems. Both wet-event types require interpretation in their local climatic and ecological context.

Environmental differences further separated loss magnitude from recovery timing. Absolute losses were greatest at low-to-intermediate elevations, whereas WC recovery was longest above 3000 m. Seasonal contrasts showed a similar separation, with DH and WC losses peaking in summer but conditional recovery taking longest in winter. Differences in baseline productivity offer a possible explanation for part of this pattern. A given proportional reduction can produce a larger absolute carbon deficit where potential assimilation is high, while a smaller deficit can persist under conditions that limit its reversal [25]. However, elevation and seasonal groups also differed in vegetation composition, event characteristics, and spatial coverage.

4.2. Environmental Predictors and Interactions Associated with GPP Responses

The predictor analysis identified different environmental associations for negative-response occurrence and cumulative loss. VPD had greater relative SHAP importance in the DH occurrence model than in the DH loss model, where contributions were distributed more evenly among VPD, soil texture, and precipitation. The more varied rankings for WH, DC, and WC likewise indicate that the fitted models used environmental information differently across event types and response metrics. Physiological explanations for these patterns are treated as hypotheses informed by the literature.

Spatial variation in predictor importance suggests that local environmental conditions help distinguish GPP losses in the fitted models. VPD ranked first across much of the DH mapping domain, whereas WH showed a mixture of soil texture, precipitation and elevation contributions. Wankmüller et al. (2024) linked soil texture and soil hydraulic conductivity to the onset of ecosystem water limitation [40]. Such hydraulic differences offer a possible explanation for the spatial associations with soil texture identified here. The VPD–precipitation interaction further shows that their contributions to predicted loss were non-additive. Variation in atmospheric water demand and concurrent water input offers a possible ecological interpretation. The positive and negative interaction signs describe the fitted response surface and do not demonstrate physiological amplification or buffering.

The WH cumulative GPP loss model had a higher independent spatial-test R^2 with the full predictor set (0.405) than when VPD (0.376) or radiation (0.300) was excluded. Mean R^2 across the five spatial cross-validation folds followed the same ordering. These results support retaining the full predictor set for prediction and interpreting individual contributions in the context of the fitted multivariable model [57].

4.3. Uncertainties and Implications for Productivity Assessments

Sensitivity analyses support the national contrasts in event exposure and GPP response. Across the 10th/90th, 15th/85th, and 20th/80th percentile definitions, the rankings remained WC > DH > WH > DC for frequency, DC > DH > WC > WH for negative-response probability, and DH > WC > DC > WH for conditional cumulative loss (Figure S1). Thus, the greater frequency of WC, the greater loss of DH, and the higher response probability but smaller loss of DC relative to WC persisted. The threshold choice nevertheless changed effect magnitudes, eligible spatial coverage, and some regional rankings. Recovery criteria affected estimated

times but preserved the national numerical ordering DH > DC > WH > WC. Requiring one, three, or five consecutive days with $Z > -0.5$ increased mean recovery time for all four event types, from 3.17 to 5.30 and 6.86 days for DH, and from 2.30 to 3.70 and 4.51 days for WC (Table S5). Stricter criteria reduced the number of recovered events and eligible pixels. The ordering also persisted on pixels eligible under all three criteria within each event type. These comparisons describe successful recoveries within the search window. Interruptions and censoring can preferentially exclude slower recoveries, so the conditional means do not estimate recovery duration for all affected events. The event window also determines which part of the productivity response is measured. Declines preceding formal onset mean that event-period losses can include continuing antecedent stress and cannot be attributed exclusively to the compound threshold crossing. Losses after termination are excluded from this metric, so it represents only part of a prolonged stress episode.

Future research could extend this framework by examining the complete sequence of vegetation responses before, during, and after compound events. Incorporating antecedent ecosystem conditions, event duration, post-event climate, and the timing of subsequent disturbances would help distinguish immediate suppression from legacy effects and incomplete recovery. Recovery could also be represented using survival or multistate approaches that account for interrupted and censored variation [58,59]. Linking these temporal processes with vegetation traits, rooting depth, land management, and physiological observations would provide a stronger basis for identifying why similar hydroclimatic events produce contrasting responses among ecosystems. At longer timescales, integrating event frequency, affected area, signed GPP anomalies, and post-event losses would clarify how individual events accumulate to influence annual and multiyear vegetation productivity.

Despite these constraints, the study provides a basis for evaluating compound events through multiple, complementary response dimensions. Areas with large absolute losses are relevant to carbon uptake, whereas areas with slower recovery may experience persistent functional impairment despite smaller immediate deficits. Neither dimension alone fully characterizes vulnerability. Extending the analysis to annual productivity effects will require integrating event frequency, affected area, signed GPP anomalies, and losses beyond the event period. Positive responses and consecutive events must also be retained in that accounting. Such an extension would connect the event-scale contrasts identified here with regional productivity changes without treating conditional losses as an estimate of net ecosystem carbon balance.

5. Conclusions

This study compared the occurrence and GPP responses of dry–hot, wet–hot, dry–cold, and wet–cold events across China from 2001 to 2025. WC events were most frequent, whereas DH combined a high negative-response probability with the largest conditional event-period GPP loss and the longest conditional recovery time. DH and DC had negative-response probabilities of 63.5% and 67.1%, with mean cumulative losses of 2.85 and 1.15 g C m^{-2} among negative-response events. WH had the lowest probability and conditional loss, at 39.9% and 0.83 g C m^{-2}. WC had a conditional loss of 1.56 g C m^{-2} and the highest observed recovery fraction (85.1%), with a conditional mean recovery time of 2.30 days. These contrasts distinguish event occurrence, response probability, conditional loss, and observed recovery as separate dimensions of vegetation response.

These contrasts demonstrate that event frequency, response probability, loss magnitude, and recovery represent separate dimensions of compound-event risk. Increasing event severity generally raised the probability and magnitude of GPP decline, but the strength of this relationship differed among event types. Responses also varied across climate regions, moisture regimes, vegetation types, and phenological stages. Dry–hot and dry–

cold losses were generally greater in water-limited environments, while the effects of wet events depended more strongly on regional hydroclimatic conditions. The predictor analysis identified further differences in their environmental associations. VPD contributed most strongly to dry–hot response probability and was also important for dry–hot losses, whereas radiation, precipitation, and soil texture played larger roles for the other event types.

These findings show that the ecological consequences of climate variability are determined jointly by the characteristics of compound events and the sensitivity of the ecosystems they affect. This distinction is essential for translating shifts in hydroclimatic extremes into realistic assessments of terrestrial carbon-cycle risk. Incorporating event exposure, productivity loss, and recovery into regional monitoring could improve the early identification of vulnerable ecosystems and provide a stronger basis for sustaining terrestrial carbon uptake through targeted adaptation and vegetation management.

Supplementary Materials: The following supporting information can be downloaded at: https://www.mdpi.com/article/10.3390/rs18213788/s1, Figure S1: Sensitivity of compound-event occurrence and vegetation responses to climate percentile thresholds; Table S1: National means and direct pairwise comparisons; Table S2: Recovery outcomes among negative-response events; Table S3: Independent spatial-test performance of the negative-response classification models; Table S4: Independent spatial-test performance of the GPP loss and recovery time regression models; Table S5: National conditional mean recovery time (days) under alternative recovery requirements.

Author Contributions: Conceptualization, P.L. and R.L.; data curation, P.L. and S.H.; formal analysis, P.L., R.L., W.G., and F.Z.; funding acquisition, C.W. and R.L.; methodology, P.L., S.H., and C.W.; project administration, P.L. and R.L.; resources, S.H.; supervision, R.L. and C.W.; visualization, P.L.; writing—original draft, P.L. and R.L.; writing—review and editing, C.W. and S.H. All authors have read and agreed to the published version of the manuscript.

Funding: This research was funded by Major Science and Technology Special Projects and Key R & D Projects in Yunnan Province in 2024 (No. 202403ZC380001) and Science and Technology Project of Department of Natural Resources of Yunnan Province (2025-YNZRKJ-009).

Data Availability Statement: The input datasets used in this study are publicly available. The Daily FluxSat GPP of biomass over Land, Based on MODIS Terra and Aqua adjusted reflectance Collection 6.1 dataset is available from ORNL DAAC (https://disc.gsfc.nasa.gov/datasets/FluxSatMGPP_L3_Daily_p05deg_2.2/summary, accessed on 8 June 2026). MODIS MCD12Q1 land-cover and SRTM elevation data are accessible through NASA Earthdata (https://www.earthdata.nasa.gov/centers/lp-daac, accessed on 8 June 2026). ERA5-Land meteorological data are available from the Copernicus Climate Data Store (https://cds.climate.copernicus.eu/datasets/reanalysis-era5-land, accessed on 10 June 2026). Root-zone soil-moisture data are available from GLEAM (https://www.gleam.eu/, accessed on 9 June 2026). Soil texture data are available from the Harmonized World Soil Database (https://www.fao.org/soils-portal/data-hub/soil-maps-and-databases/harmonized-world-soil-database-v12/en/, accessed on 15 July 2026).

Acknowledgments: The numerical calculations in this paper were performed on the supercomputing system at the Supercomputing Center of Wuhan University.

Conflicts of Interest: The authors declare no conflicts of interest.

Abbreviations

The following abbreviations are used in this manuscript:

DC	Dry–cold
DH	Dry–hot
ERA5	Fifth-generation ECMWF reanalysis
ERA5-Land	Land component of the fifth-generation ECMWF reanalysis
GPP	Gross primary productivity
LightGBM	Light Gradient Boosting Machine

SHAP	Shapley Additive Explanations
VPD	Vapor pressure deficit
WC	Wet–cold
WH	Wet–hot

References

1. Beer, C.; Reichstein, M.; Tomelleri, E.; Ciais, P.; Jung, M.; Carvalhais, N.; Rödenbeck, C.; Arain, M.A.; Baldocchi, D.; Bonan, G.B.; et al. Terrestrial Gross Carbon Dioxide Uptake: Global Distribution and Covariation with Climate. *Science* **2010**, *329*, 834–838. [CrossRef] [PubMed]
2. Jung, M.; Reichstein, M.; Schwalm, C.R.; Huntingford, C.; Sitch, S.; Ahlström, A.; Arneth, A.; Camps-Valls, G.; Ciais, P.; Friedlingstein, P.; et al. Compensatory water effects link yearly global land CO2 sink changes to temperature. *Nature* **2017**, *541*, 516–520. [CrossRef] [PubMed]
3. Piao, S.; Wang, X.; Park, T.; Chen, C.; Lian, X.; He, Y.; Bjerke, J.W.; Chen, A.; Ciais, P.; Tømmervik, H.; et al. Characteristics, drivers and feedbacks of global greening. *Nat. Rev. Earth Environ.* **2020**, *1*, 14–27. [CrossRef]
4. Zscheischler, J.; Mahecha, M.D.; von Buttlar, J.; Harmeling, S.; Jung, M.; Rammig, A.; Randerson, J.T.; Schölkopf, B.; Seneviratne, S.I.; Tomelleri, E.; et al. A few extreme events dominate global interannual variability in gross primary production. *Environ. Res. Lett.* **2014**, *9*, 035001. [CrossRef]
5. Stocker, B.D.; Zscheischler, J.; Keenan, T.F.; Prentice, I.C.; Seneviratne, S.I.; Peñuelas, J. Drought impacts on terrestrial primary production underestimated by satellite monitoring. *Nat. Geosci.* **2019**, *12*, 264–270. [CrossRef]
6. Grossiord, C.; Buckley, T.N.; Cernusak, L.A.; Novick, K.A.; Poulter, B.; Siegwolf, R.T.W.; Sperry, J.S.; McDowell, N.G. Plant responses to rising vapor pressure deficit. *New Phytol.* **2020**, *226*, 1550–1566. [CrossRef] [PubMed]
7. Liu, L.; Gudmundsson, L.; Hauser, M.; Qin, D.; Li, S.; Seneviratne, S.I. Soil moisture dominates dryness stress on ecosystem production globally. *Nat. Commun.* **2020**, *11*, 4892. [CrossRef] [PubMed]
8. Wang, J.; Hua, H.; Guo, J.; Huang, X.; Zhang, X.; Yang, Y.; Wang, D.; Guo, X.; Zhang, R.; Smith, N.G.; et al. Late spring frost delays tree spring phenology by reducing photosynthetic productivity. *Nat. Clim. Chang.* **2025**, *15*, 201–209. [CrossRef]
9. Luo, H.; Bastos, A.; Reichstein, M.; Duveiller, G.; Kretzschmar, J.; Quaas, J. Hydroclimate shapes photosynthetic sensitivity to cloud cover across global terrestrial ecosystems. *Nat. Commun.* **2026**, *17*, 1646. [CrossRef] [PubMed]
10. Ridder, N.N.; Pitman, A.J.; Westra, S.; Ukkola, A.; Do, H.X.; Bador, M.; Hirsch, A.L.; Evans, J.P.; Di Luca, A.; Zscheischler, J. Global hotspots for the occurrence of compound events. *Nat. Commun.* **2020**, *11*, 5956. [CrossRef] [PubMed]
11. Chen, Y.; Wang, G.; Seth, A. Climatic Drivers for the Variation of Gross Primary Productivity Across Terrestrial Ecosystems in the United States. *J. Geophys. Res. Biogeosci.* **2024**, *129*, e2024JG008168. [CrossRef]
12. Zscheischler, J.; Westra, S.; van den Hurk, B.J.J.M.; Seneviratne, S.I.; Ward, P.J.; Pitman, A.; AghaKouchak, A.; Bresch, D.N.; Leonard, M.; Wahl, T.; et al. Future climate risk from compound events. *Nat. Clim. Chang.* **2018**, *8*, 469–477. [CrossRef]
13. Zscheischler, J.; Martius, O.; Westra, S.; Bevacqua, E.; Raymond, C.; Horton, R.M.; van den Hurk, B.; AghaKouchak, A.; Jézéquel, A.; Mahecha, M.D.; et al. A typology of compound weather and climate events. *Nat. Rev. Earth Environ.* **2020**, *1*, 333–347. [CrossRef]
14. Liu, M.; Yu, H.; Duan, W.; Wu, M. Differential impacts of compound dry- and humid-hot events on global vegetation productivity. *Front. Environ. Sci.* **2025**, *13*, 1597553. [CrossRef]
15. Cheng, X.; Zhan, C.; De Kauwe, M.G.; Hildebrandt, A.; Orth, R. Global vegetation responses to wet and dry soil moisture extremes. *Biogeosciences* **2026**, *23*, 5117–5131. [CrossRef]
16. Gampe, D.; Zscheischler, J.; Reichstein, M.; O'Sullivan, M.; Smith, W.K.; Sitch, S.; Buermann, W. Increasing impact of warm droughts on northern ecosystem productivity over recent decades. *Nat. Clim. Chang.* **2021**, *11*, 772–779. [CrossRef]
17. Seneviratne, S.I.; Corti, T.; Davin, E.L.; Hirschi, M.; Jaeger, E.B.; Lehner, I.; Orlowsky, B.; Teuling, A.J. Investigating soil moisture–climate interactions in a changing climate: A review. *Earth Sci. Rev.* **2010**, *99*, 125–161. [CrossRef]
18. Li, J.; Bevacqua, E.; Wang, Z.; Sitch, S.; Arora, V.; Arneth, A.; Jain, A.K.; Goll, D.; Tian, H.; Zscheischler, J. Hydroclimatic extremes contribute to asymmetric trends in ecosystem productivity loss. *Commun. Earth Environ.* **2023**, *4*, 197. [CrossRef]
19. Huang, S.; Wang, S.; Wang, C.; Zhang, X.; Gong, J.; Chen, N. Soil moisture deficits amplify and prolong vegetation productivity losses under compound dry-hot extremes. *Innov. Geosci.* **2026**, *4*, 100235. [CrossRef]
20. Zhang, Y.; Chen, X.; Geng, S.; Zhang, X. A review of soil waterlogging impacts, mechanisms, and adaptive strategies. *Front. Plant Sci.* **2025**, *16*, 1545912. [CrossRef] [PubMed]
21. Zong, X.; Liu, Y.; Yin, Y. Identifying the dominant compound events and their impacts on vegetation growth in China. *Weather Clim. Extrem.* **2024**, *45*, 100715. [CrossRef]

22. Wang, H.; Yan, S.; Ciais, P.; Wigneron, J.P.; Liu, L.; Li, Y.; Fu, Z.; Ma, H.; Liang, Z.; Wei, F.; et al. Exploring complex water stress–gross primary production relationships: Impact of climatic drivers, main effects, and interactive effects. *Glob. Chang. Biol.* **2022**, *28*, 4110–4123. [CrossRef] [PubMed]
23. Bastos, A.; Sippel, S.; Frank, D.; Mahecha, M.D.; Zaehle, S.; Zscheischler, J.; Reichstein, M. A joint framework for studying compound ecoclimatic events. *Nat. Rev. Earth Environ.* **2023**, *4*, 333–350. [CrossRef]
24. Bai, Y.H.; Chen, J.; Zhang, Y.W.; Tang, Z. Response Modes of Global Vegetation to Extreme Drought. *Glob. Chang. Biol.* **2025**, *31*, e70488. [CrossRef] [PubMed]
25. Schwalm, C.R.; Anderegg, W.R.L.; Michalak, A.M.; Fisher, J.B.; Biondi, F.; Koch, G.; Litvak, M.; Ogle, K.; Shaw, J.D.; Wolf, A.; et al. Global patterns of drought recovery. *Nature* **2017**, *548*, 202–205. [CrossRef] [PubMed]
26. Zhang, S.; Yang, Y.; Wu, X.; Li, X.; Shi, F. Postdrought Recovery Time Across Global Terrestrial Ecosystems. *J. Geophys. Res. Biogeosci.* **2021**, *126*, e2020JG005699. [CrossRef]
27. Yao, Y.; Liu, Y.; Zhou, S.; Song, J.; Fu, B. Soil moisture determines the recovery time of ecosystems from drought. *Glob. Chang. Biol.* **2023**, *29*, 3562–3574. [CrossRef] [PubMed]
28. Shi, P.; Sun, S.; Wang, M.; Li, N.; Wang, J.A.; Jin, Y.; Gu, X.; Yin, W. Climate change regionalization in China (1961–2010). *Sci. China Earth Sci.* **2014**, *57*, 2676–2689. [CrossRef]
29. Huang, L.; Chen, J.; Yang, K.; Yang, Y.; Huang, W.; Zhang, X.; Chen, F. The northern boundary of the Asian summer monsoon and division of westerlies and monsoon regimes over the Tibetan Plateau in present-day. *Sci. China Earth Sci.* **2023**, *66*, 882–893. [CrossRef]
30. Chen, W.; Zhu, D.; Huang, C.; Ciais, P.; Yao, Y.; Friedlingstein, P.; Sitch, S.; Haverd, V.; Jain, A.K.; Kato, E.; et al. Negative extreme events in gross primary productivity and their drivers in China during the past three decades. *Agric. For. Meteorol.* **2019**, *275*, 47–58. [CrossRef]
31. Joiner, J.; Yoshida, Y. *Global MODIS and FLUXNET-Derived Daily Gross Primary Production, V2*; ORNL DAAC: Oak Ridge, TN, USA, 2021. [CrossRef]
32. Joiner, J.; Yoshida, Y.; Zhang, Y.; Duveiller, G.; Jung, M.; Lyapustin, A.; Wang, Y.; Tucker, C.J. Estimation of Terrestrial Global Gross Primary Production (GPP) with Satellite Data-Driven Models and Eddy Covariance Flux Data. *Remote Sens.* **2018**, *10*, 1346. [CrossRef]
33. Sulla-Menashe, D.; Gray, J.M.; Abercrombie, S.P.; Friedl, M.A. Hierarchical mapping of annual global land cover 2001 to present: The MODIS Collection 6 Land Cover product. *Remote Sens. Environ.* **2019**, *222*, 183–194. [CrossRef]
34. Muñoz-Sabater, J.; Dutra, E.; Agustí-Panareda, A.; Albergel, C.; Arduini, G.; Balsamo, G.; Boussetta, S.; Choulga, M.; Harrigan, S.; Hersbach, H.; et al. ERA5-Land: A state-of-the-art global reanalysis dataset for land applications. *Earth Syst. Sci. Data* **2021**, *13*, 4349–4383. [CrossRef]
35. Miralles, D.G.; Bonte, O.; Koppa, A.; Baez-Villanueva, O.M.; Tronquo, E.; Zhong, F.; Beck, H.E.; Hulsman, P.; Dorigo, W.; Verhoest, N.E.C.; et al. GLEAM4: Global land evaporation and soil moisture dataset at 0.1° resolution from 1980 to near present. *Sci. Data* **2025**, *12*, 416. [CrossRef] [PubMed]
36. Farr, T.G.; Rosen, P.A.; Caro, E.; Crippen, R.; Duren, R.; Hensley, S.; Kobrick, M.; Paller, M.; Rodriguez, E.; Roth, L.; et al. The Shuttle Radar Topography Mission. *Rev. Geophys.* **2007**, *45*, RG2004. [CrossRef]
37. FAO; IIASA; ISRIC; ISSCAS; JRC. *Harmonized World Soil Database (Version 1.2)*; FAO: Rome, Italy; IIASA: Laxenburg, Austria, 2012. Available online: https://www.fao.org/soils-portal/data-hub/soil-maps-and-databases/harmonized-world-soil-database-v12/en/ (accessed on 15 July 2026).
38. Ke, G.; Meng, Q.; Finley, T.; Wang, T.; Chen, W.; Ma, W.; Ye, Q.; Liu, T.-Y. LightGBM: A Highly Efficient Gradient Boosting Decision Tree. In *Advances in Neural Information Processing Systems*; Curran Associates, Inc.: Red Hook, NY, USA, 2017; Volume 30, pp. 3146–3154. Available online: https://proceedings.neurips.cc/paper_files/paper/2017/hash/6449f44a102fde848669bdd9eb6b76fa-Abstract.html (accessed on 20 July 2026).
39. Fu, Z.; Ciais, P.; Prentice, I.C.; Gentine, P.; Makowski, D.; Bastos, A.; Luo, X.; Green, J.K.; Stoy, P.C.; Yang, H.; et al. Atmospheric dryness reduces photosynthesis along a large range of soil water deficits. *Nat. Commun.* **2022**, *13*, 989. [CrossRef] [PubMed]
40. Wankmüller, F.J.P.; Delval, L.; Lehmann, P.; Baur, M.J.; Cecere, A.; Wolf, S.; Or, D.; Javaux, M.; Carminati, A. Global influence of soil texture on ecosystem water limitation. *Nature* **2024**, *635*, 631–638. [CrossRef] [PubMed]
41. Perkins, S.E.; Alexander, L.V. On the Measurement of Heat Waves. *J. Clim.* **2013**, *26*, 4500–4517. [CrossRef]
42. Bevacqua, E.; De Michele, C.; Manning, C.; Couasnon, A.; Ribeiro, A.F.S.; Ramos, A.M.; Vignotto, E.; Bastos, A.; Blesić, S.; Durante, F.; et al. Guidelines for Studying Diverse Types of Compound Weather and Climate Events. *Earth's Future* **2021**, *9*, e2021EF002340. [CrossRef]
43. Saito, M.; Kato, T.; Tang, Y. Temperature controls ecosystem CO2 exchange of an alpine meadow on the northeastern Tibetan Plateau. *Glob. Chang. Biol.* **2009**, *15*, 221–228. [CrossRef]
44. Shi, W.; Zhang, K.; Huang, S.; Huang, Y.; Xie, Y.; Li, Y.; Liu, L.; Forzieri, G. Widespread declining sensitivity of terrestrial gross primary productivity to compound dry-hot extremes in China. *J. Hydrol.* **2025**, *660*, 133387. [CrossRef]

45. Frank, D.; Reichstein, M.; Bahn, M.; Thonicke, K.; Frank, D.; Mahecha, M.D.; Smith, P.; van der Velde, M.; Vicca, S.; Babst, F.; et al. Effects of climate extremes on the terrestrial carbon cycle: Concepts, processes and potential future impacts. *Glob. Chang. Biol.* **2015**, *21*, 2861–2880. [CrossRef] [PubMed]
46. Yao, Y.; Fu, B.; Liu, Y.; Zhang, Y.; Ding, J.; Li, Y.; Zhou, S.; Song, J.; Wang, S.; Li, C.; et al. Compound hot–dry events greatly prolong the recovery time of dryland ecosystems. *Natl. Sci. Rev.* **2024**, *11*, nwae274. [CrossRef] [PubMed]
47. Wei, D.; Tao, J.; Wang, Z.; Zhao, H.; Zhao, W.; Wang, X. Elevation-dependent pattern of net CO2 uptake across China. *Nat. Commun.* **2024**, *15*, 2489. [CrossRef] [PubMed]
48. Gu, X.; Wang, R.; Chen, D.; Miao, C.; Luo, S.; Guan, Y.; Wang, S.; Li, L.; Gu, T.; Luo, C.; et al. Multilayer soil moisture depletion intensifies drought impacts on global ecosystems. *Nat. Geosci.* **2026**, *19*, 1205–1212. [CrossRef] [PubMed]
49. Sun, Y.; Guan, Q.; Du, Q.; Wang, Q.; Sun, W. Elevation dependence of vegetation growth stages and carbon sequestration dynamics in high mountain ecosystems. *Environ. Res.* **2025**, *273*, 121200. [CrossRef] [PubMed]
50. Zou, L.; Zhu, W.; Xia, J.; Wang, F.; She, D.; Liu, C.; Xu, J.; Zuo, L. Precipitation and shortwave radiation dominate vegetation recovery times from flash droughts across Köppen–Geiger climate zones. *Agric. For. Meteorol.* **2026**, *388*, 111325. [CrossRef]
51. Ciais, P.; Reichstein, M.; Viovy, N.; Granier, A.; Ogée, J.; Allard, V.; Aubinet, M.; Buchmann, N.; Bernhofer, C.; Carrara, A.; et al. Europe-wide reduction in primary productivity caused by the heat and drought in 2003. *Nature* **2005**, *437*, 529–533. [CrossRef] [PubMed]
52. Drake, J.E.; Tjoelker, M.G.; Vårhammar, A.; Medlyn, B.E.; Reich, P.B.; Leigh, A.; Pfautsch, S.; Blackman, C.J.; López, R.; Aspinwall, M.J.; et al. Trees tolerate an extreme heatwave via sustained transpirational cooling and increased leaf thermal tolerance. *Glob. Chang. Biol.* **2018**, *24*, 2390–2402. [CrossRef] [PubMed]
53. Lu, M.; Sun, H.; Yang, Y.; Xue, J.; Ling, H.; Zhang, H.; Zhang, W. Assessing recovery time of ecosystems in China: Insights into flash drought impacts on gross primary productivity. *Hydrol. Earth Syst. Sci.* **2025**, *29*, 613–625. [CrossRef]
54. von Buttlar, J.; Zscheischler, J.; Rammig, A.; Sippel, S.; Reichstein, M.; Knohl, A.; Jung, M.; Menzer, O.; Arain, M.A.; Buchmann, N.; et al. Impacts of droughts and extreme-temperature events on gross primary production and ecosystem respiration: A systematic assessment across ecosystems and climate zones. *Biogeosciences* **2018**, *15*, 1293–1318. [CrossRef]
55. Bastos, A.; Ciais, P.; Friedlingstein, P.; Sitch, S.; Pongratz, J.; Fan, L.; Wigneron, J.P.; Weber, U.; Reichstein, M.; Fu, Z.; et al. Direct and seasonal legacy effects of the 2018 heat wave and drought on European ecosystem productivity. *Sci. Adv.* **2020**, *6*, eaba2724. [CrossRef] [PubMed]
56. Peng, J.; Tang, J.; Xie, S.; Wang, Y.; Liao, J.; Chen, C.; Sun, C.; Mao, J.; Zhou, Q.; Niu, S. Evidence for the acclimation of ecosystem photosynthesis to soil moisture. *Nat. Commun.* **2024**, *15*, 9795. [CrossRef] [PubMed]
57. Aas, K.; Jullum, M.; Løland, A. Explaining individual predictions when features are dependent: More accurate approximations to Shapley values. *Artif. Intell.* **2021**, *298*, 103502. [CrossRef]
58. Kaplan, E.L.; Meier, P. Nonparametric Estimation from Incomplete Observations. *J. Am. Stat. Assoc.* **1958**, *53*, 457–481. [CrossRef]
59. Putter, H.; Fiocco, M.; Geskus, R.B. Tutorial in biostatistics: Competing risks and multi-state models. *Stat. Med.* **2007**, *26*, 2389–2430. [CrossRef] [PubMed]

Disclaimer/Publisher's Note: The statements, opinions and data contained in all publications are solely those of the individual author(s) and contributor(s) and not of MDPI and/or the editor(s). MDPI and/or the editor(s) disclaim responsibility for any injury to people or property resulting from any ideas, methods, instructions or products referred to in the content.